nature portfolio

https://doi.org/10.1038/s41557-021-00688-0

## Supplementary information

# Constructing ion channels from water-soluble α-helical barrels

In the format provided by the authors and unedited

# Methods and Supplementary Information for:

# "Constructing ion-channels from water-soluble α-helical barrels"

Alistair J. Scott, Ai Niitsu, Huong T. Kratochvil, Eric J. M. Lang, Jason T. Sengel, William M. Dawson, Kozhinjampara. R. Mahendran, Marco Mravic, Andrew R. Thomson, R. Leo Brady, Lijun Liu, Adrian J. Mulholland, Hagan Bayley, William F. DeGrado, Mark I. Wallace, and Derek N. Woolfson

Correspondence to: d.n.woolfson@bristol.ac.uk

**Index**

## Computational methods

bZIP Interface Scoring

Complementary pairs of coiled-coil interfaces were identified using the bZIP[1] scoring function, as previously described[2]. Briefly, bZIP generates a unitless estimate of coiled-coil pairing energy based on the g, a, d, and e register positions, with positive scores representing more favourable pairings. By searching for pairings that score well in combination, but where the individual homo-pairings score poorly, it is possible to identify homotypic interface pairs. Where there is a suitable overlap in sequence composition, it is possible to combine these interface pairs into a single sequence that when folded into a helix displays each interface on either side of that helix. This arrangement gives rise to barrel-like assemblies. The bZIP function has access to pairing energy values for polar a and d residues, as well as hydrophobic residues at the e and g positions. Therefore, we reasoned that bZIP scores could be used as the basis of sequence designs for 'inverted' Type-2 interfaces with a polar core and hydrophobic periphery. Type-2 interfaces where a = Thr and d = Ser were scored. Positions b and c were limited to L, I or V. Fitness scores for interface pairs were assigned by subtracting the score for the highest-scoring competing homo-assembly from that of the desired heteromeric assembly. For scores see Supplementary Table 3.

Molecular dynamics (MD) simulations of water-soluble barrels

System preparation

Starting from the crystal structures of CC-Type2-$(T_aS_d)_2$ (PDB ID: 6YB0), CC-Type2-$(T_aI_d)_5$ (PDB ID: 6YAZ) and CC-Type2-$(L_aI_dS_g)_2$ (CC-Hex2; PDB ID: 4PN9), missing residues CC-Type2-$(T_aI_d)_5$ were modelled using the automodel routine of Modeller[3] with other residues kept fixed and a helical restraint applied to residues 2 to 36. Of the 25 models created, the one with the best molpdf score was retained. For CC-Type2-$(L_aI_dS_g)_2$ (CC-Hex2), the missing Gly residues were modelled in with COOT[4] as described previously[5]. For all three structures, crystallographic water molecules were retained, and Maestro's Protein Preparation Wizard (Schrödinger Release 2017-4: Maestro, Schrödinger, LLC, New York, NY, 2017) was used to choose between possible flipped Gln conformations; to cap *N*-and *C*-terminus residues with acetyl and amine moieties, respectively; to add hydrogen atoms using the protonation states calculated with Propka[6]; and optimising the hydrogen bonds network. The resulting structures were then solvated with the SOLVATE program (http://www.mpibpc.mpg.de/grubmueller/solvate, last visited November 2019), developed by H. Grubmüller and V. Groll, to create a solvation shell of TIP3P water molecules of at least 5 Å around the protein using 8 Gaussians. The tleap program, part of the Amber 17 modelling suite[7] was then used to create a truncated octahedron cell of TIP3P water molecules setting the padding to 6 Å around the previously generated solvation shell and the closeness to 0.75 Å. $K^+$ and $Cl^-$ ions were added randomly to the solvent cell to neutralise the protein charge and model a concentration of 0.1 M KCl. The protein was modelled using the Amber ff14SB force field[8].

MD simulations

For each system, 3 replicas were run, each starting with different randomly assigned Boltzmann velocity distribution. For each replica, we followed the same careful minimisation-heating-equilibration protocol established previously[5]. Briefly, the system was minimised, first restraining the non-hydrogen protein atoms, then only the backbone atoms with a decreasing harmonic restraint, then only the Cα atoms and finally without any restraints. Heating was achieved by linearly increasing the temperature from 0 to 293 K over 20 ps, restraining the backbone atoms using a force constant of 5 $kcal.mol^{-1}.Å^{-2}$. NPT equilibration was then run, first gradually decreasing the restraint on the backbone atoms from 5 to 1 $kcal.mol^{-1}.Å^{-2}$ over 3 steps of 500 ps, then gradually decreasing the restraint on the Cα from 1 to 0.05 $kcal.mol^{-1}.Å^{-2}$ over 5 steps of 500 ps. Equilibration was then pursued for 5 ns without any restraints.

Production MD was then run in the NPT ensemble, with 3 replicas simulated for 500 ns for each system. For both equilibration and production phases, temperature was kept at 293 K using Langevin dynamics with a thermostat collision of 5 $ps^{-1}$ and pressure was maintained constant with a MC barostat using a relaxation time of 1 ps.

Apart from the minimisation and heating phases that were run with pmemd.MPI, all the simulations were run using pmemd.CUDA[9], part of the Amber 17 modelling suite[7], on single Nvidia P100 GPUs available on the University of Bristol HPC system BlueCrystal Phase 4.

MD Analysis

Trajectories were processed with CPPTRAJ[10], part of the Amber 17 modelling suite[7], removing the protein translational and rotational motions, calculating the backbone RMSD and the water density inside the channels (grid command). MD structure figures and movies were prepared with VMD[11].

The channels and their water content were then analysed using the Channel Annotation Package CHAP (https://www.channotation.org/, last visited November 2019[12]). For the analysis, the 3 replica simulations for each system were concatenated and the CHAP analysis was run every 30 ps of the 1.5 μs trajectories. The cut-off applied to the minimum water number density, *n min*, to evaluate if the channel exhibit or not a continuous line of interacting water molecules along the channel, connecting the bulk water at the two ends was determined empirically by comparing *n min* for various degrees of channel occupancy. For CC-Type2-$(T_aI_d)_5$ and CC-Type2-$(T_aS_d)_2$ a cut-off value of 12.275 (corresponding to 1 $k_BT$ of energy barrier between water in the pore and the bulk) and 8.342 (corresponding to ¼ of the bulk density number of water) were chosen respectively. The cut-off is different for the two systems due to the difference in shape and volume for the two channels. Our choice for the cut-off was reinforced by the fact that those values correspond approximatively to the antimode of the near bimodal distribution of the minimum number density for CC-Type2-$(T_aI_d)_5$ and for the short hydrophobic region of CC-Type2-$(T_aS_d)_2$ (Supplementary Figure 48).

Molecular dynamics (MD) simulations of CCTM-$V_bI_c$

Bilayer System Set-up

Starting from the octameric biological assembly from the crystal structures of $K_2$-CCTM-$V_bI_c$ (PDB: 6YB1), the protein was embedded and oriented in the bilayer using CHARMM-GUI[13] with the CHARMM36m[14] parameters. Crystallographic water molecules were removed. The initial bilayer orientation was predicted using the OPM ppm server[15], from water-octanol transfer energies. The protein was embedded in a 95 Å square 1,2-diphytanoyl-*sn*-glycero-3-phosphocholine (DPhPC) lipid patch and solvated an additional 27.5 Å of TIP3P water molecules in the z-direction of the bilayer, resulting in 101 and 102 lipids in the upper and lower leaflet, respectively. Ions were added by replacing water molecules to neutralize the system and result in a final salt concentration of 1 M of either KCl, NaCl or $CaCl_2$. The final unequilibrated box dimensions were 95 x 95 x 108 Å with 93500 – 93810 atoms, depending on the ion. GROMACS was used for minimization and molecular dynamics using the recommended cut-off, switching, and Particle-Mesh Ewald distances for CHARMM36m, with a 2 fs time step for Langevin dynamics.

The system was minimized using 5000 steps using steepest decent with harmonic positional restraints on all non-hydrogen protein atoms using 4 kcal $mol^{-1}$ $Å^{-2}$ for backbone atoms and 2 kcal $mol^{-1}$ $Å^{-2}$ for sidechain atoms. A 50 ps NVT dynamics simulation was next conducted using similar restraints, with temperature controlled at 293 K with the V-rescale algorithm and a 0.1 ps coupling constant. A 20 ns NPT dynamics simulation was next run with 1 kcal $mol^{-1}$ $Å^{-2}$ harmonic restraints on protein Cα atoms, with a Berendsen thermostat at 293 K with a 1.0 ps coupling constant and a semiisotropic Berendsen barostat at 1 bar with a pressure coupling time constant of 1 ps. Finally, unrestrained dynamics simulations were conducted with a Nose-Hoover thermostat at 293 K with a 1.0 ps coupling constant and a semiisotropic Parrinello-Rahman barostat at 1 bar with a pressure

coupling time constant of 1 ps. The trajectories containing KCl, NaCl and $CaCl_2$ were run for 700 ns, 2 μs and 500 ns, respectively. The systems' time-averaged dimensions were approximately 92 x 92 x 106 Å.

Water residency analysis

The 2 μs unrestrained MD simulation of $K_2$-CCTM-$V_bI_c$ was analysed to assess the occupancy and residence time of water molecules at the major polar hydrated sites within the two interiors formed by the outer four-helix bundle (the central bundle remained dry throughout the simulation). The first 240 ns were discarded as equilibration and frames were analysed every 120 ps (>16000 frames analysed in total).

For each frame, the CCTM core (residues 4-30) was aligned to that of the protein medoid conformation of the trajectory (obtained after clustering the protein trajectory using a k-medoids algorithm). From a subset of ~500 frames uniformly distributed across 240 ns to 2 μs, the centroid position of water molecules nearby each of the designated water sites (6 sites per tetrameric pore, 12 sites total, Supplementary Figure 58) was calculated. Each water site centroid calculation included >500 waters limited to within a 1.2 Å radius of the centroid position.

These centroid positions were then used to track individual water molecules entering and exiting those water sites as well as their dwell time (Supplementary Figure 60, Table 5). A water was considered bound within a water site if it was within 2 Å of the defined water site centroid and if it was the closest water to that site and closer to that site than to any other sites.

Modelling electrostatic energy profiles and I-V curves

System preparation

Parallel and antiparallel hexameric models of $K_2$-CCTM-$V_bI_c$ were prepared with CCBuilder 2.0[16] using the crystallographic parameters of CC-Type2-$(T_aS_d)_2$ (radius = 9.31 Å, interface angle = 13.98° and pitch = 168.1 Å). To test the influence of the channel radius on the results, a parallel hexameric model of $K_2$-CCTM-$V_bI_c$ optimized by CCBuilder 2.0 was considered, with the default optimization procedure leading to a narrower channel with the following parameters: radius = 8.9 Å, interface angle = 17.3° and pitch = 320 Å. The peptides were capped at the *C* and *N* terminus and hydrogen atoms were added with PDB2PQR[17].

Electrostatics calculations

To calculate the electrostatics energy profile of ions translocation through the CCTM channels, the APBS program[17] was used to solve nonlinear Poisson-Boltzmann (PB) equation. The effect of the phospholipid bilayer was accounted for using APBSmem[18]. The total thickness of the lipid bilayer was set to 36.3 Å and the polar head group thickness to 4.25 Å, to match experimental measurements[19]. Dielectric constants of 2 and 25 were used for the hydrophobic part of the lipid bilayer and the polar head groups respectively[20], 3 was used for the protein[21], and 78.5 for water (including the inside of the channels). The protein was oriented with the channel axis aligned along the z axis and the center z = 0 was chosen to be the geometric center of all the Trp side chains, thereby corresponding to the center of the lipid bilayer since the Trp side chains were used to position the protein relative to the bilayer[22] in agreement with the PPM webserver[15] (Supplementary Figure 61). To calculate the electrostatic potential energy profile of $K^+$ and $Cl^-$ moving through the channel, the ions were moved along the z axis between -40 and 40 Å by 0.5 Å increments and the electrostatic component of the energy calculated at each step using the same procedure as described in[23]. The Swanson parameter set for the charges and radii [24] was used for the protein as it yields smoother energy profiles for ion translocation [23] and the Roux radii were used for $K^+$ and $Cl^-$[25]. Given that the peptides were inserted experimentally in the presence of a +100 mV potential, the orientation of the parallel hexamer under those conditions were determined by running PB calculations run with APBSmem in the presence of a membrane potential ("Gating charge" calculations) (Supplementary Figure 62). Unsurprisingly, the peptide with the *C* terminus on the same side to which the potential is applied is the favoured orientation under a +100 mV

potential, with the positively charged Lys residues at the *N* terminus being on the 0 mV side (as shown in Supplementary Figure 61).

Modelling of I-V curves

Assuming the fluxes of the anions and cations inside a channel are independent, current-voltage curves were qualitatively modelled using Nernst-Planck equation for electrodiffusion[26]. The equation was solved using a similar approach than used in previous work[27,28], relying on the calculated electrostatic energy profiles of ion passage through the channel, with the total calculated current given by:

$$I_{calc} = F[C]\left(\left(\beta_c \frac{exp(v_c FV/RT) - 1}{\int_{-l/2}^{l/2} \frac{exp(v_c F\phi_c(z)/RT)}{D_c(z)\pi r(z)^2} dz}\right) + \left(\beta_a \frac{exp(v_a FV/RT) - 1}{\int_{-l/2}^{l/2} \frac{exp(v_a F\phi_a(z)/RT)}{D_a(z)\pi r(z)^2} dz}\right)\right) \quad (1)$$

where $F$ is the Faraday constant; $R$ the gas constant; $T$ the absolute temperature; $[C]$ the salt concentration, 1M (equals on both sides of the membrane); $V$ is the applied potential; $r(z)$ is the radius of the channel along the channel axis (z-axis) and is calculated with HOLE[29]; $l$ is the length of the channel centered on z=0; $v_c$ is the cation valence (+1); $D_c(z)$ the diffusion coefficient for cations within the channel, $\beta_c$ is the partition coefficient for cations from the bulk solution into the channel; and $\phi_c(z)$ is the electrostatic potential for the cation at position z. $v_a, D_a(z), \beta_a$ and $\phi_a(z)$ are the corresponding quantities for anions.

To simplify the calculations, we made a number of assumptions. Firstly, the length of the channel is considered to be equal to the lipid bilayer thickness, $l = l_{mem} = 36.3$ Å, that is only the transmembrane region of the peptide is considered. This was chosen to minimize the incertitude arising from the flexibility of the peptide regions outside the membrane, which can have a significant effect on the channel radius and electrostatic potential for those regions. Secondly, because we considered the channel to be hydrated and have the same dielectric constant as bulk water, the water-channel partition coefficients were chosen to be equal to 1, $\beta_c = \beta_a = 1$. Finally, we considered the applied voltage on one side of the membrane to drop linearly to 0 along the channel.

The electrostatic potential at position z for the cations or anions, $\phi_{c/a}(z)$, is given by:

$$\phi_{c/a}(z) = \psi_{a/c}(z) + \mathcal{V}(z) \quad (2)$$

where $\psi_{a/c}(z)$ is the electrostatic potential energy profile of ion translocation through the channel calculated with APBS; and $\mathcal{V}(z)$, illustrated in Supplementary Figure 63, describe the evolution of the applied potential $V$ along the z coordinates (following the convention established in Supplementary Figure 61) and is define as:

$$\mathcal{V}(z) = \begin{cases} V, & z < -\frac{l_{mem}}{2} \\ V \times \left(\frac{1}{2} - \frac{1}{l_{mem}}\right) \times z, & -\frac{l_{mem}}{2} \le z \le \frac{l_{mem}}{2} \\ 0, & z > \frac{l_{mem}}{2} \end{cases} \quad (3)$$

and because we chose $l = l_{mem}$, Eq. 3 simplifies as follow:

$$\mathcal{V}(z) = V \times \left(\frac{1}{2} - \frac{1}{l}\right) \times z \tag{4}$$

Compared to previous approaches[27,28] where bulk ion diffusion coefficients were used, $D_{c/a}(z)$ is calculated the diffusion along the channel[30] which gives more accurate results than using the bulk value, even for narrow channels[31]. It is defined as:

$$D_{c/a}(z) = \frac{D_{c/a}^{Bulk}}{0.64309 + 0.00044 \times exp\left(\frac{r_{c/a}}{0.06894 \times r(z)}\right) + 0.35647 \times exp\left(\frac{r_{c/a}}{0.19409 \times r(z)}\right)} \tag{5}$$

where $D_{c/a}^{Bulk}$ is the bulk diffusion coefficient and equals to $1.96 \times 10^{-5}$ cm$^2$/s and $2.03 \times 10^{-5}$ cm$^2$/s for $K^+$ and $Cl^-$ respectively [26]; $r(z)$ is the channel radius; and $r_{c/a}$ is the radius of the ions and equals 1.7638 and 2.27 for $K^+$ and $Cl^-$ respectively [25].

As in[27], a single variable multiplying the calculated current was used to fit the experimental data:

$$I_{fit} = cI_{calc} \tag{6}$$

This fitting procedure was preferred over a 2-variable fitting procedure (with one variable for cation current and one for anion) used to avoid artificially dictating the relative weight of the $K^+$ and $Cl^-$ fluxes that could arise.

## HPLC and MALDI-TOF data

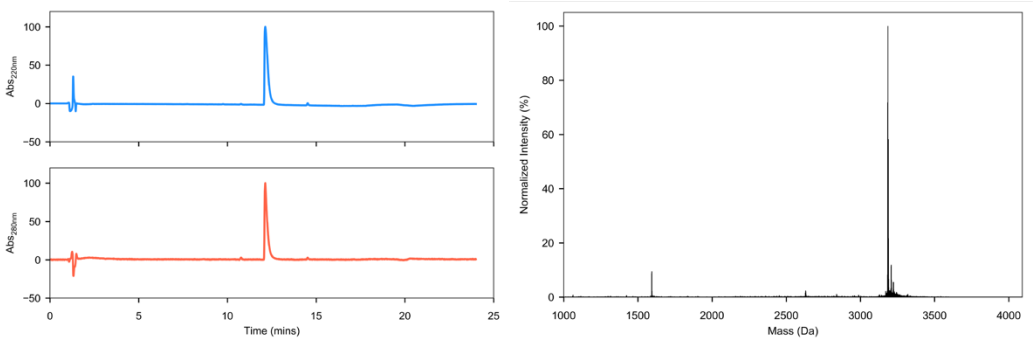


**Figure 1. CC-Type2-($T_aI_d$)$_2$ -** HPLC traces (left) from a linear gradient of 20 to 80% MeCN (0.1% TFA) in $H_2O$ (0.1% TFA), monitored at 220 nm (blue) and 280 nm (red). MALDI-TOF mass spectrum (right). Calculated monoisotopic peptide mass = 3220.8 Da, observed mass = 3222 Da.

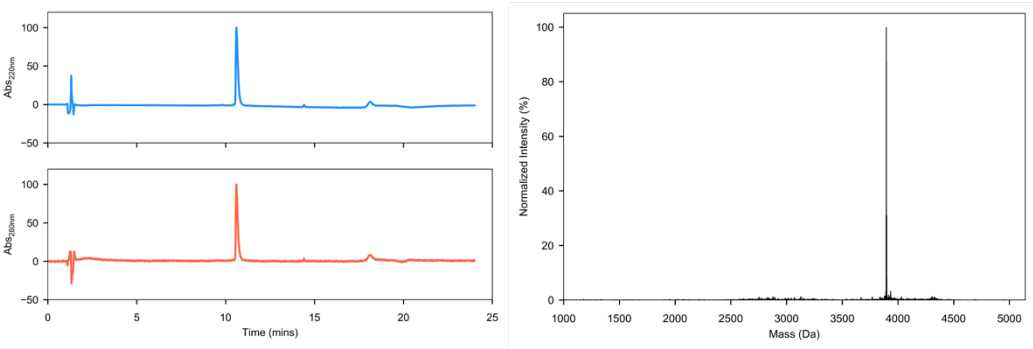


**Figure 2. CC-Type2-($T_aI_d$)$_5$ -** HPLC traces (left) from a linear gradient of 20 to 80% MeCN (0.1% TFA) in $H_2O$ (0.1% TFA), monitored at 220 nm (blue) and 280 nm (red). MALDI-TOF mass spectrum (right). Calculated monoisotopic peptide mass = 3938.1 Da, observed mass = 3940 Da.

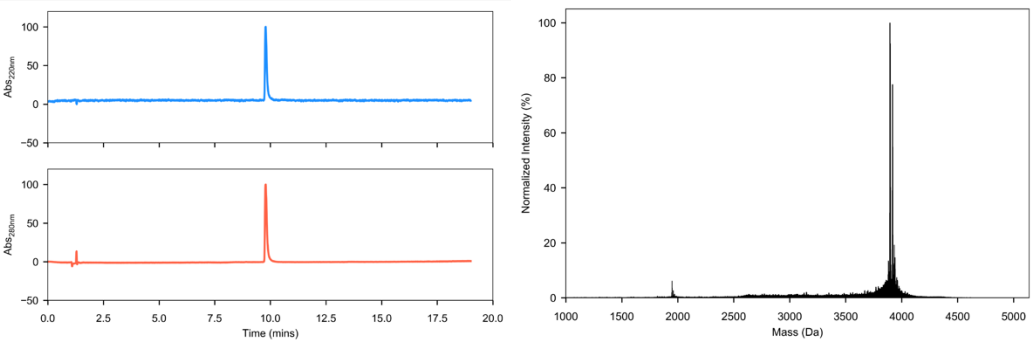


**Figure 3. CC-Type2-($L_aT_d$)$_5$ -** HPLC traces (left) from a linear gradient of 20 to 80% MeCN (0.1% TFA) in $H_2O$ (0.1% TFA), monitored at 220 nm (blue) and 280 nm (red). MALDI-TOF mass spectrum (right). Calculated monoisotopic peptide mass = 3938.1 Da, observed mass = 3940 Da.

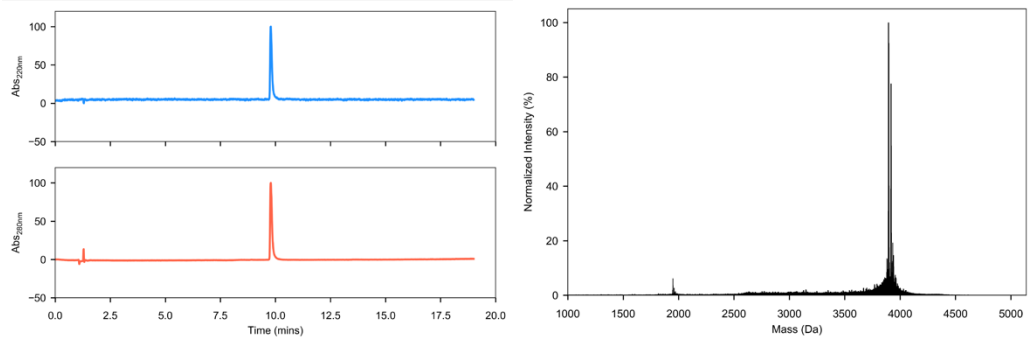


**Figure 4. CC-Type2-($S_aI_d$)$_5$ -** HPLC traces (left) from a linear gradient of 20 to 80% MeCN (0.1% TFA) in $H_2O$ (0.1% TFA), monitored at 220 nm (blue) and 280 nm (red). MALDI-TOF mass spectrum (right). Calculated monoisotopic peptide mass = 3868.1 Da, observed mass = 3871 Da.

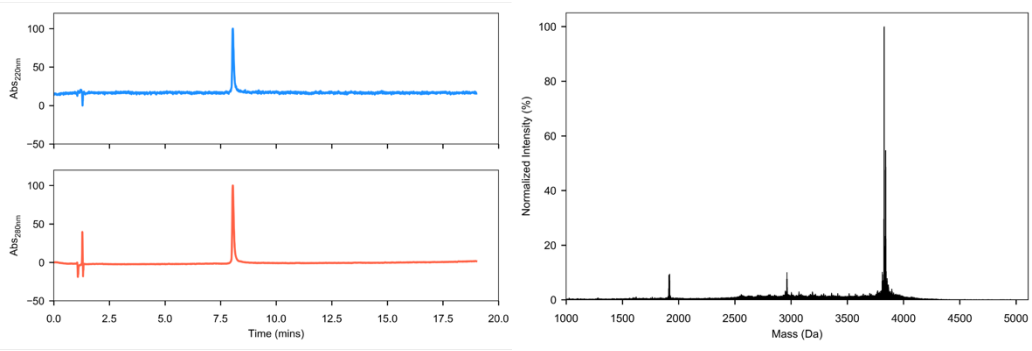


**Figure 5. CC-Type2-($L_aS_d$)$_5$ -** HPLC traces (left) from a linear gradient of 20 to 80% MeCN (0.1% TFA) in $H_2O$ (0.1% TFA), monitored at 220 nm (blue) and 280 nm (red). MALDI-TOF mass spectrum (right). Calculated monoisotopic peptide mass = 3868.1 Da, observed mass = 3871 Da.

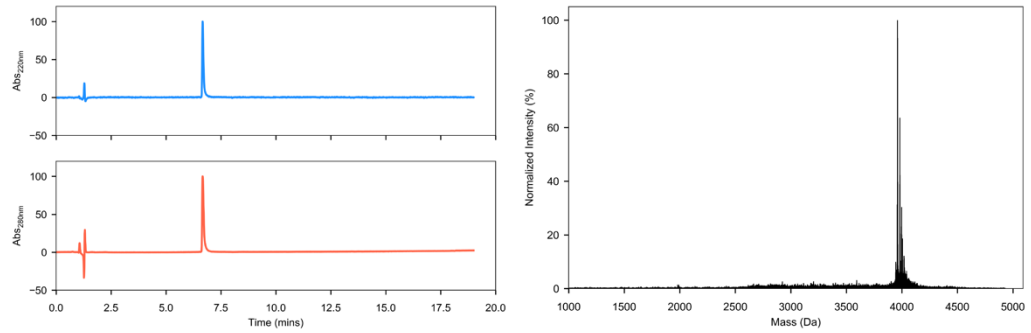


**Figure 6. CC-Type2-($L_aN_d$)$_5$ -** HPLC traces (left) from a linear gradient of 20 to 80% MeCN (0.1% TFA) in $H_2O$ (0.1% TFA), monitored at 220 nm (blue) and 280 nm (red). MALDI-TOF mass spectrum (right). Calculated monoisotopic peptide mass = 4003.1 Da, observed mass = 4005 Da.

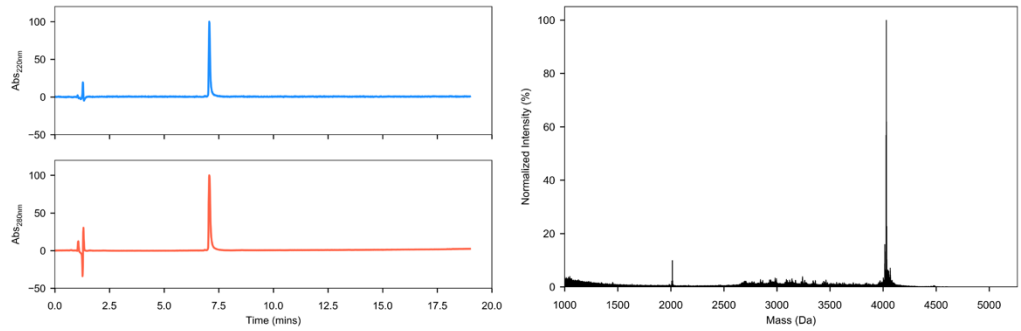


**Figure 7. CC-Type2-($L_aQ_d)_5$ -** HPLC traces (left) from a linear gradient of 20 to 80% MeCN (0.1% TFA) in $H_2O$ (0.1% TFA), monitored at 220 nm (blue) and 280 nm (red). MALDI-TOF mass spectrum (right). Calculated monoisotopic peptide mass = 4073.1 Da, observed mass = 4078 Da.

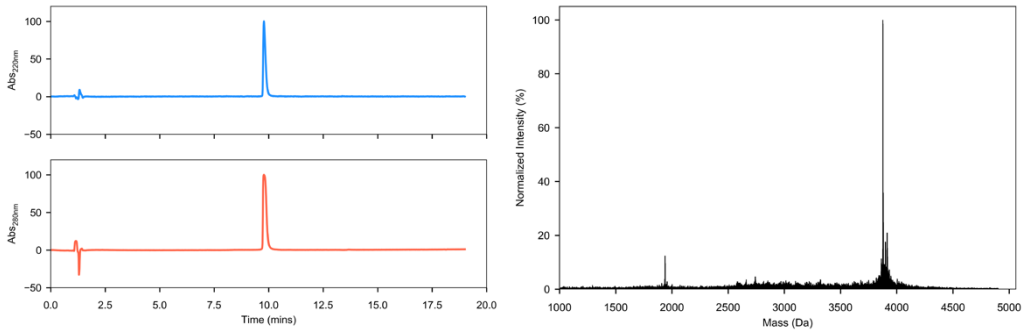


**Figure 8. CC-Type2-($T_aS_d)_2$ -** HPLC traces (left) from a linear gradient of 20 to 80% MeCN (0.1% TFA) in $H_2O$ (0.1% TFA), monitored at 220 nm (blue) and 280 nm (red). MALDI-TOF mass spectrum (right). Calculated monoisotopic peptide mass = 3922.1 Da, observed mass = 3922 Da.

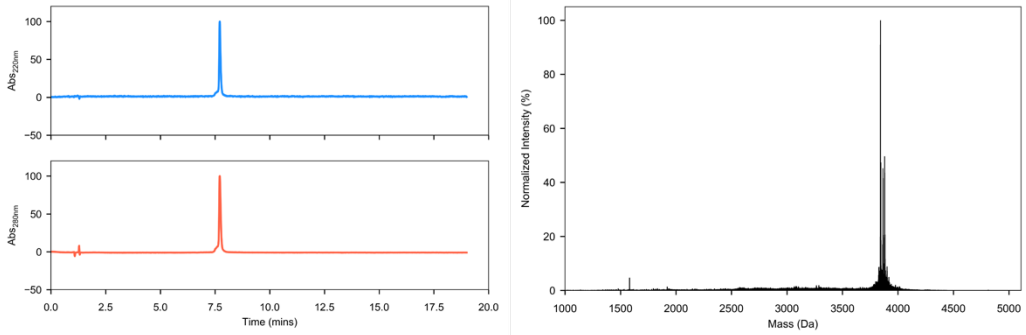


**Figure 9. CC-Type2-($T_aS_d)_3$ -** HPLC traces (left) from a linear gradient of 20 to 80% MeCN (0.1% TFA) in $H_2O$ (0.1% TFA), monitored at 220 nm (blue) and 280 nm (red). MALDI-TOF mass spectrum (right). Calculated monoisotopic peptide mass = 3884.0 Da, observed mass = 3887 Da.

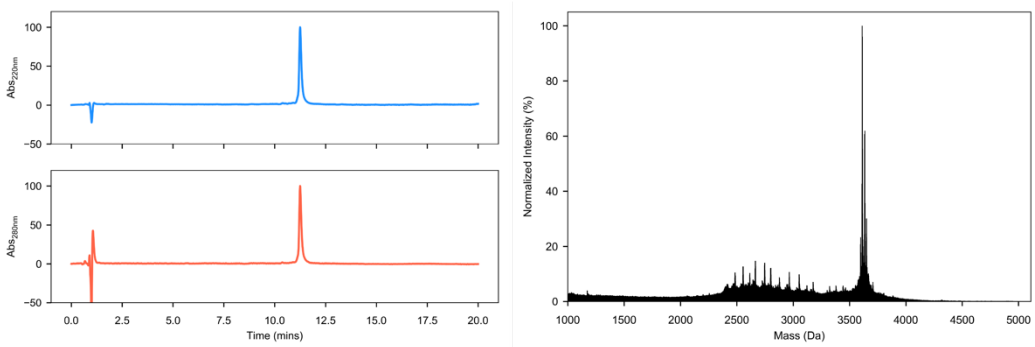


**Figure 10. CCTM-$L_bL_c$ -** HPLC traces (left) from a linear gradient of 40 to 100% IPA:MeCN:$H_2O$ (60:30:10, 0.1% TFA) in $H_2O$ (0.1% TFA), monitored at 220 nm (blue) and 280 nm (red). MALDI-TOF mass spectrum (right). Calculated monoisotopic peptide mass = 3653.1 Da, observed mass = 3655 Da.

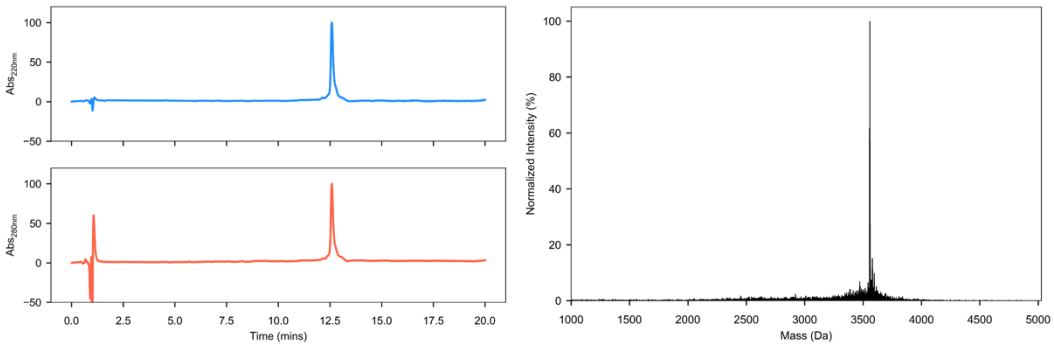


**Figure 11. CCTM-$V_bI_c$ -** HPLC traces (left) from a linear gradient of 40 to 100% IPA:MeCN:$H_2O$ (60:30:10, 0.1% TFA) in $H_2O$ (0.1% TFA), monitored at 220 nm (blue) and 280 nm (red). MALDI-TOF mass spectrum (right). Calculated monoisotopic peptide mass = 3597.0 Da, observed mass = 3600 Da.

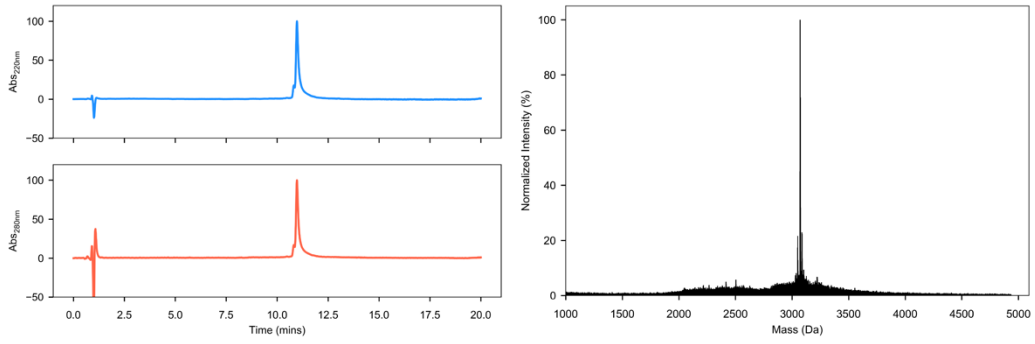


**Figure 12. $K_2$-CCTM-$V_bI_c$ -** HPLC traces (left) from a linear gradient of 40 to 100% IPA:MeCN:$H_2O$ (60:30:10, 0.1% TFA) in $H_2O$ (0.1% TFA), monitored at 220 nm (blue) and 280 nm (red). MALDI-TOF mass spectrum (right). Calculated monoisotopic peptide mass = 3083.7 Da, observed mass = 3085 Da.

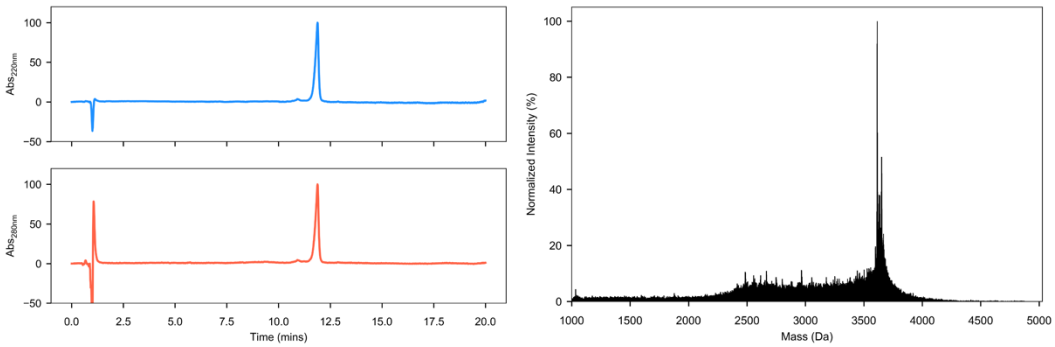


**Figure 13. CCTM-$I_bI_c$ -** HPLC traces (left) from a linear gradient of 40 to 100% IPA:MeCN:$H_2O$ (60:30:10, 0.1% TFA) in $H_2O$ (0.1% TFA), monitored at 220 nm (blue) and 280 nm (red). MALDI-TOF mass spectrum (right). Calculated monoisotopic peptide mass = 3653.1 Da, observed mass = 3656 Da.

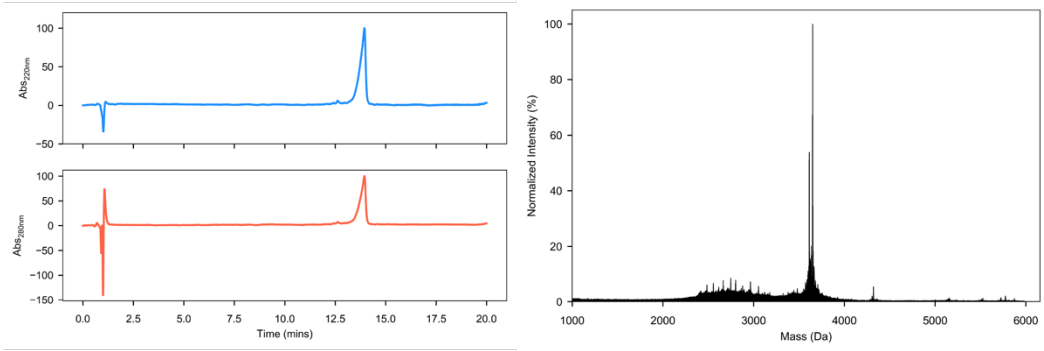


**Figure 14. CCTM-$I_bL_c$ -** HPLC traces (left) from a linear gradient of 40 to 100% IPA:MeCN:$H_2O$ (60:30:10, 0.1% TFA) in $H_2O$ (0.1% TFA), monitored at 220 nm (blue) and 280 nm (red). MALDI-TOF mass spectrum (right). Calculated monoisotopic peptide mass = 3653.1 Da, observed mass = 3654 Da.

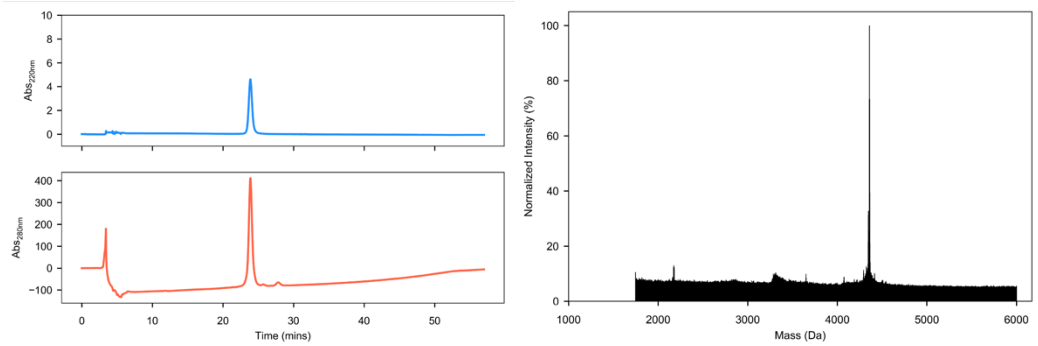


**Figure 15. Cy5-CCTM-$V_bI_c$ -** HPLC traces (left) from a linear gradient of 40 to 100% IPA in $H_2O$ (0.1% TFA), monitored at 280 nm (blue) and 600 nm (red). MALDI-TOF mass spectrum (right). Calculated monoisotopic peptide mass = 4407.3 Da, observed mass = 4411 Da.

## CD spectroscopy data

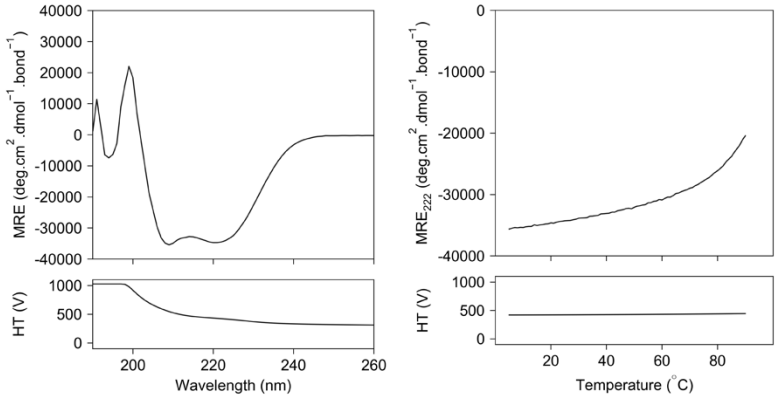


**Figure 16.** CD spectroscopy data for **CC-Type2-($T_aI_d$)$_2$**. Left: CD spectrum at 20 °C. Right: thermal denaturation profile monitored at 222 nm wavelength. Temperature gradient: 30 °C / hour. Conditions: 100 μM peptide concentration, PBS buffer, pH 7.4.

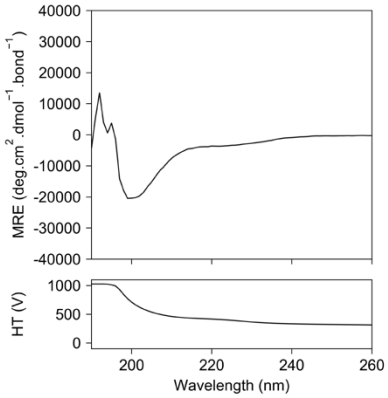


**Figure 17.** CD spectrum of **CC-Type2-($L_aT_d$)$_5$** at 20 °C. Conditions: 100 μM peptide concentration, PBS buffer, pH 7.4.

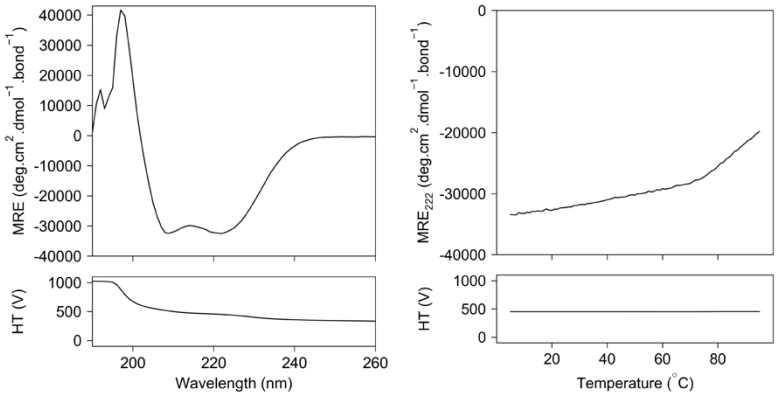


**Figure 18.** CD spectroscopy data for **CC-Type2-($L_aI_d$)$_1$($L_aT_d$)$_2$($L_aI_d$)$_1$**. Left: CD spectrum at 20 °C. Right: thermal denaturation profile monitored at 222 nm wavelength. Temperature gradient: 30 °C / hour. Conditions: 100 μM peptide concentration, PBS buffer, pH 7.4.

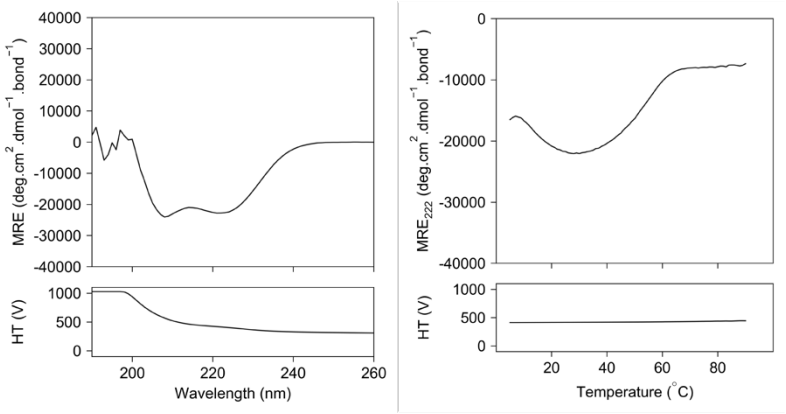


**Figure 19.** CD spectroscopy data for **CC-Type2-($T_aI_d$)$_5$**. Left: CD spectrum at 20 °C. Right: thermal denaturation profile monitored at 222 nm wavelength. Temperature gradient: 15 °C / hour. Conditions: 100 µM peptide concentration, HEPES 10 mM, KCl 100 mM, pH 7.4.

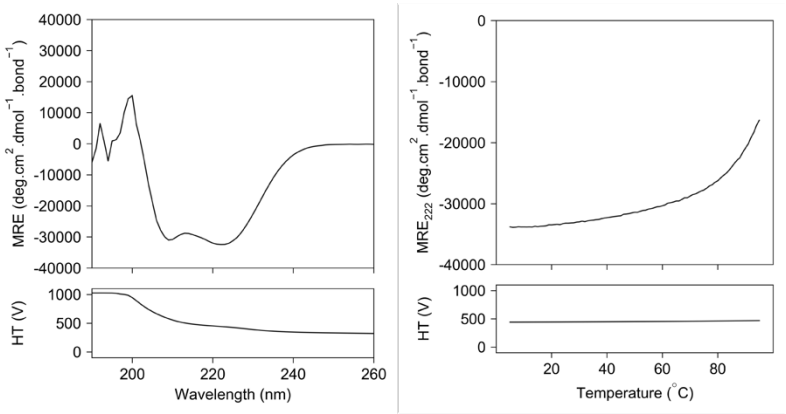


**Figure 20.** CD spectroscopy data for **CC-Type2-($L_aT_d$)$_5$**. Left: CD spectrum at 20 °C. Right: thermal denaturation profile monitored at 222 nm wavelength. Temperature gradient: 30 °C / hour. Conditions: 100 µM peptide concentration, HEPES 10 mM, KCl 100 mM, pH 7.4.

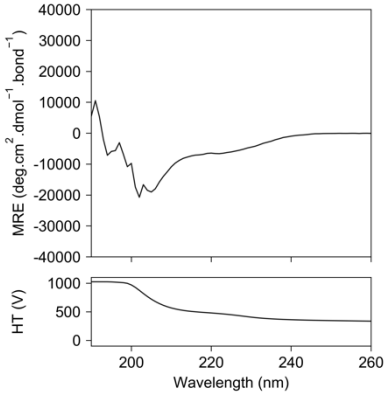


**Figure 21.** CD spectrum of **CC-Type2-($S_aI_d$)$_5$** at 20 °C. Conditions: 100 µM peptide concentration, 10 mM HEPES, 100 mM KCl, pH 7.4.

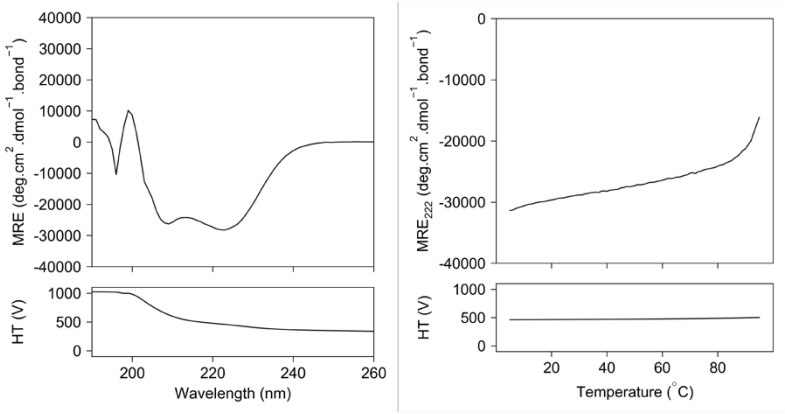


**Figure 22.** CD spectroscopy data for **CC-Type2-($L_aS_d$)$_5$**. Left: CD spectrum at 20 °C. Right: thermal denaturation profile monitored at 222 nm wavelength. Temperature gradient: 30 °C / hour. Conditions: 100 µM peptide concentration, HEPES 10 mM, KCl 100 mM, pH 7.4.

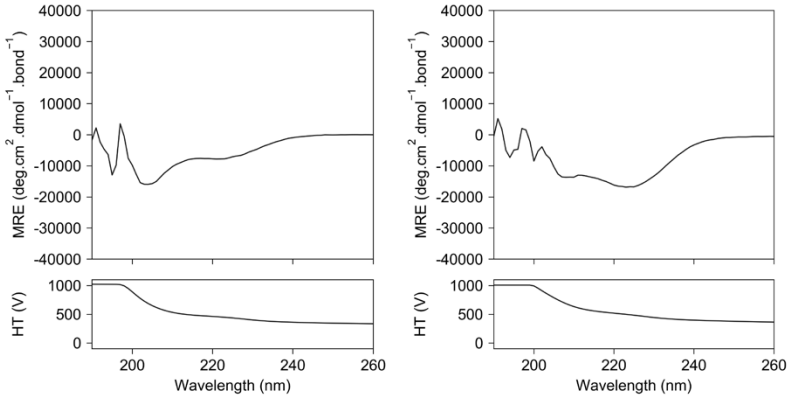


**Figure 23.** Left: CD spectrum of **CC-Type2-($L_aN_d$)$_5$** at 20 °C. Conditions: 100 µM peptide concentration, 10 mM Tris-HCl, 100 mM KCl, pH 7.4. Right: CD spectrum of **CC-Type2-LQ$_5$** at 20 °C. Conditions: 100 µM peptide concentration, 10 mM Tris, 100 mM KCl, pH 7.4. Slow precipitation was evident.

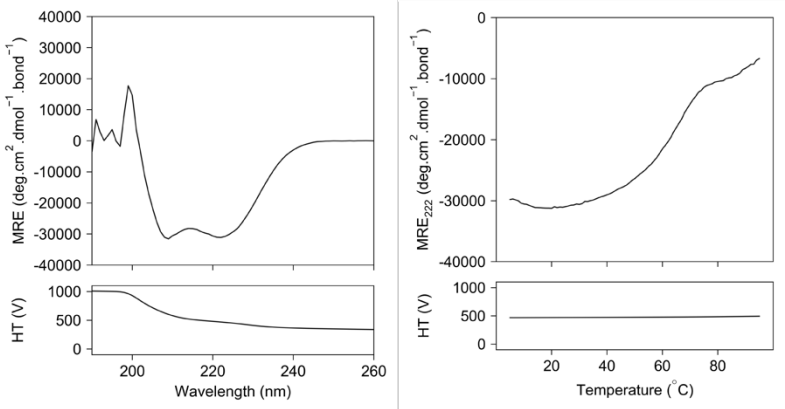


**Figure 24.** CD spectroscopy data for **CC-Type2-($T_aS_d$)$_2$**. Left: CD spectrum at 20 °C. Right: thermal denaturation profile monitored at 222 nm wavelength. Temperature gradient: 15 °C / hour. Conditions: 100 µM peptide concentration, HEPES 10 mM, KCl 100 mM, pH 7.4.

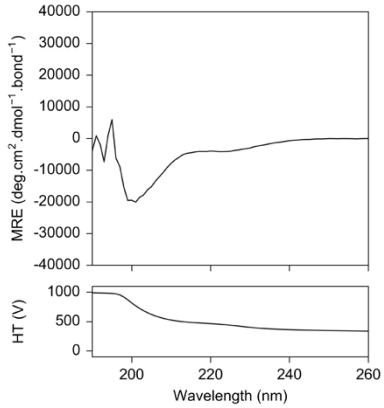


**Figure 25.** CD spectrum of **CC-Type2-($T_aS_d$)$_3$** at 20 °C. Conditions: 100 µM peptide concentration, PBS buffer, pH 7.4.

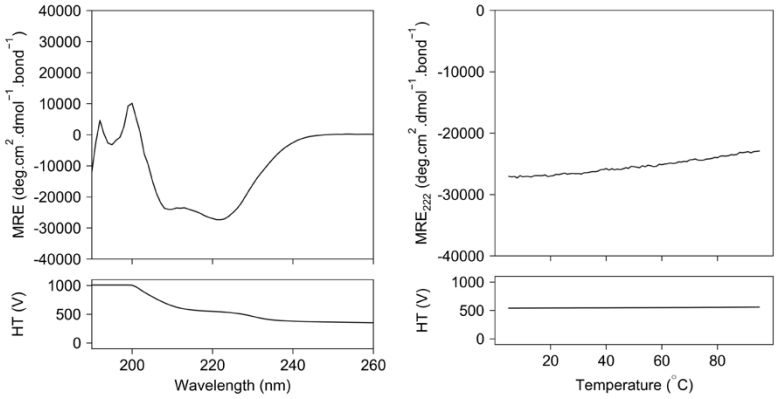


**Figure 26.** CD spectroscopy data for **CCTM-$L_bL_c$**. Left: CD spectrum at 20 °C. Right: thermal denaturation profile monitored at 222 nm wavelength. Temperature gradient: 60 °C / hour. Conditions: 100 µM peptide concentration, 0.05% DDM, HEPES 10 mM, KCl 100 mM, pH 7.4.

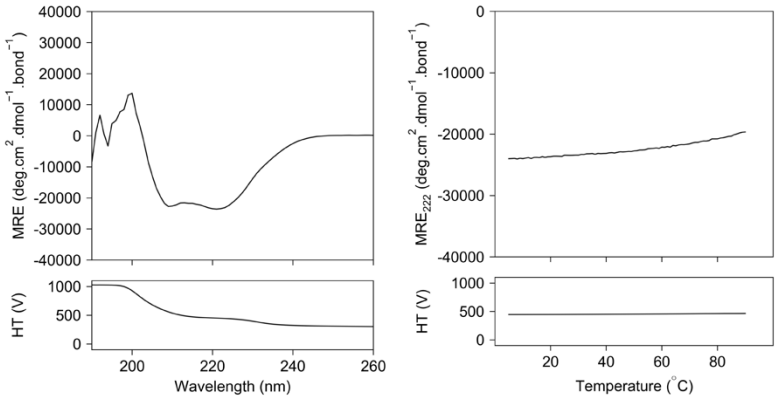


**Figure 27.** CD spectroscopy data for **CCTM-$V_bI_c$**. Left: CD spectrum at 20 °C. Right: thermal denaturation profile monitored at 222 nm wavelength. Temperature gradient: 60 °C / hour. Conditions: 100 µM peptide concentration, 0.05% DDM, HEPES 10 mM, KCl 100 mM, pH 7.4.

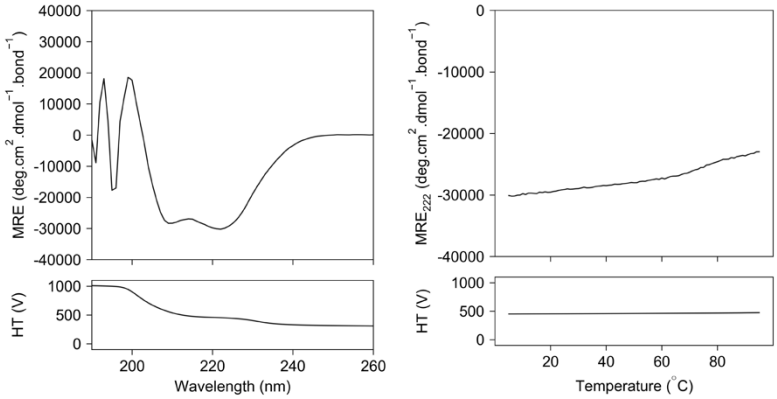


**Figure 28.** CD spectroscopy data for **$K_2$-CCTM-$V_bI_c$**. Left: CD spectrum at 20 °C. Right: thermal denaturation profile monitored at 222 nm wavelength. Temperature gradient: 60 °C / hour. Conditions: 100 µM peptide concentration, 0.05% DDM, HEPES 10 mM, KCl 100 mM, pH 7.4.

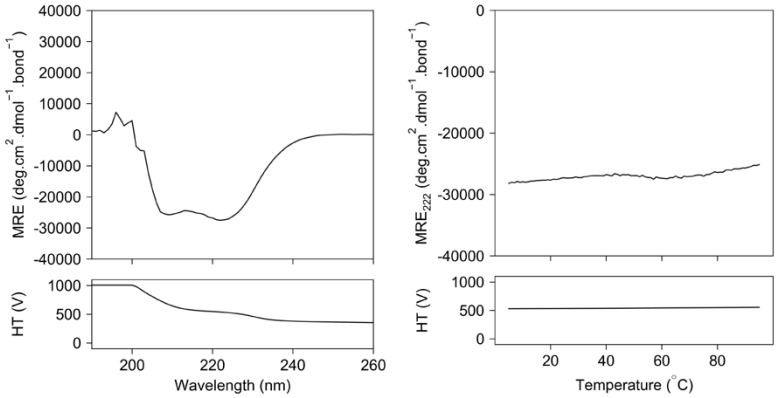


**Figure 29.** CD spectroscopy data for **CCTM-$I_bL_c$**. Left: CD spectrum at 20 °C. Right: thermal denaturation profile monitored at 222 nm wavelength. Temperature gradient: 60 °C / hour. Conditions: 100 µM peptide concentration, 0.05% DDM, HEPES 10 mM, KCl 100 mM, pH 7.4.

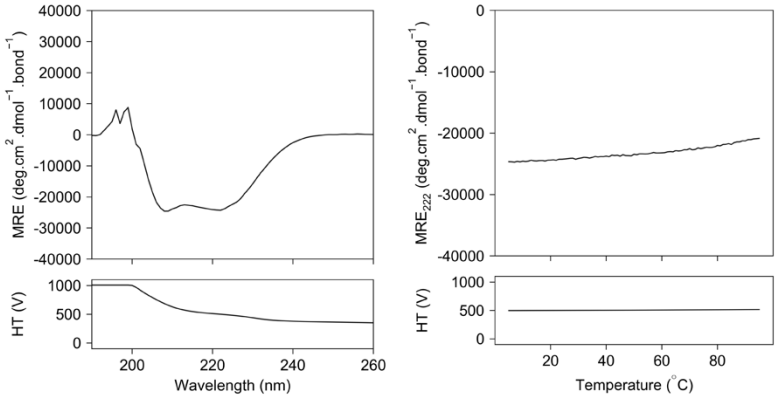


**Figure 30.** CD spectroscopy data for **CCTM-$I_bI_c$**. Left: CD spectrum at 20 °C. Right: thermal denaturation profile monitored at 222 nm wavelength. Temperature gradient: 60 °C / hour. Conditions: 100 µM peptide concentration, 0.05% DDM, HEPES 10 mM, KCl 100 mM, pH 7.4.

## AUC data

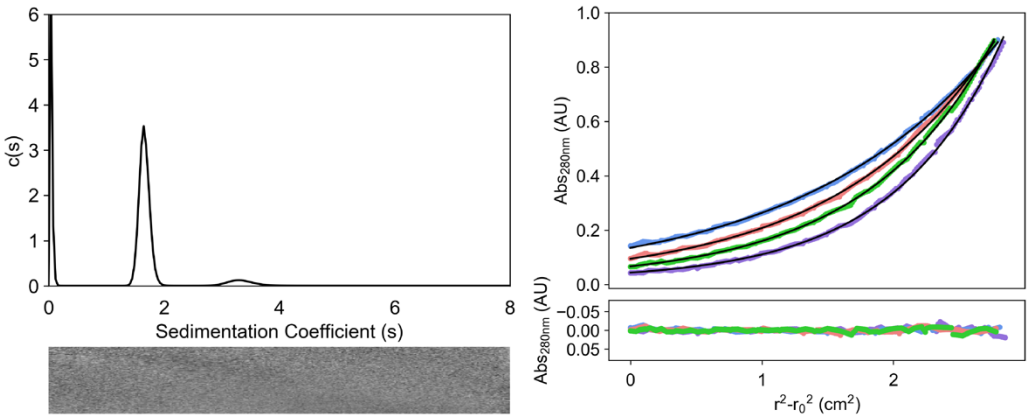


**Figure 31.** AUC data and fits (top) with residuals (bottom) for **CC-Type2-($L_aI_d$)$_1$($T_aI_d$)$_2$($L_aI_d$)$_1$** ($\bar{\nu}$ = 0.766). Left: sedimentation velocity continuous c(s) distribution at 50 krpm (s = 1.66 S, $s_{20,w}$ = 1.70 S, f/$f_0$ = 1.23, Mw = 17688 Da, 5.5x monomer mass at a 95% confidence level). Right: sedimentation equilibrium data and fitted curves from 18 – 36 krpm for a single-species model (Mw = 18124 Da, 5.6x monomer mass, 95% confidence limits 18071 – 18178 Da). Conditions: 20 °C, PBS, pH 7.4. SV and SE experiments were conducted at 150 and 75 µM concentrations, respectively.

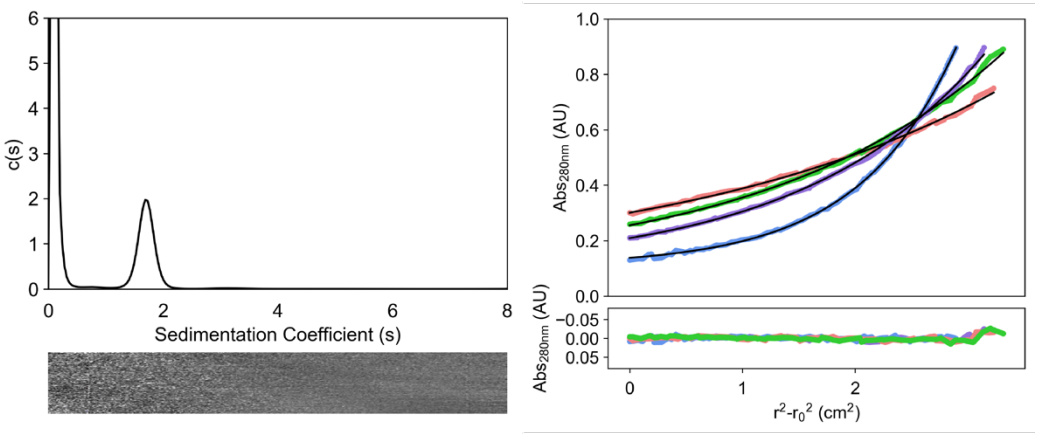


**Figure 32.** AUC data and fits (top) with residuals (bottom) for **CC-Type2-($T_aI_d$)$_5$** ($\bar{\nu}$ = 0.751). Left: sedimentation velocity continuous c(s) distribution at 50 krpm (s = 1.70 S, $s_{20,w}$ = 1.96 S, f/$f_0$ = 1.41, Mw = 24343 Da, 6.2x monomer mass at a 95% confidence level). Right: sedimentation equilibrium data and fitted curves from 15 – 33 krpm for a single-species model (Mw = 19509 Da, 5.0x monomer mass, 95% confidence limits 18919 – 19735 Da). Conditions: 20 °C, 10 mM Tris-HCl, 100 mM KCl, pH 8. SV and SE experiments were conducted at 150 and 75 µM concentrations, respectively.

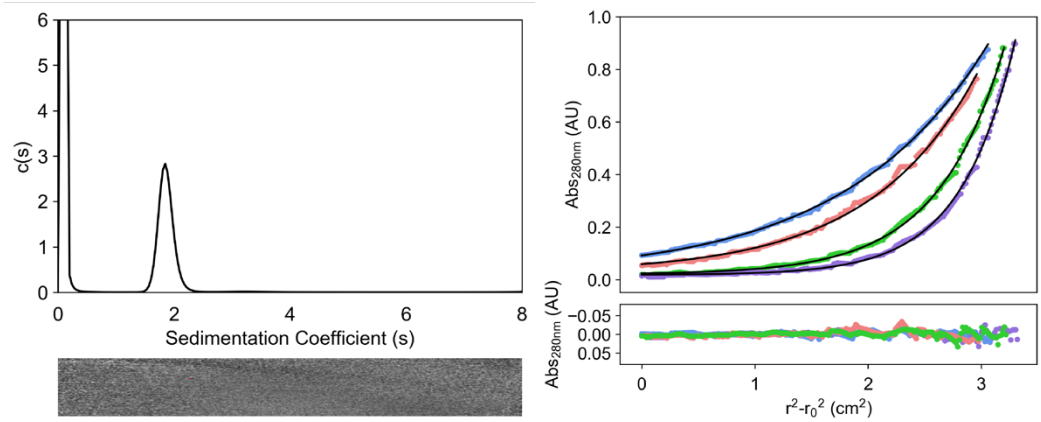


**Figure 33.** AUC data and fits (top) with residuals (bottom) for **CC-Type2-($L_aT_d$)$_5$** ($\bar{\nu}$ = 0.751**)**. Left: sedimentation velocity continuous c(s) distribution at 50 krpm (s = 1.92 S, $s_{20,w}$ = 1.95 S, f/$f_0$ = 1.30, Mw = 21197, 5.4x monomer mass at a 95% confidence level). Right: sedimentation equilibrium data and fitted curves from 18 – 36 krpm for a single-species model (Mw = 21368 Da, 5.4x monomer mass, 95% confidence limits 21003 – 21158 Da). Conditions: 20 °C, 10 mM HEPES, 100 mM KCl, pH 7.4. SV and SE experiments were conducted at 150 and 75 μM concentrations, respectively.

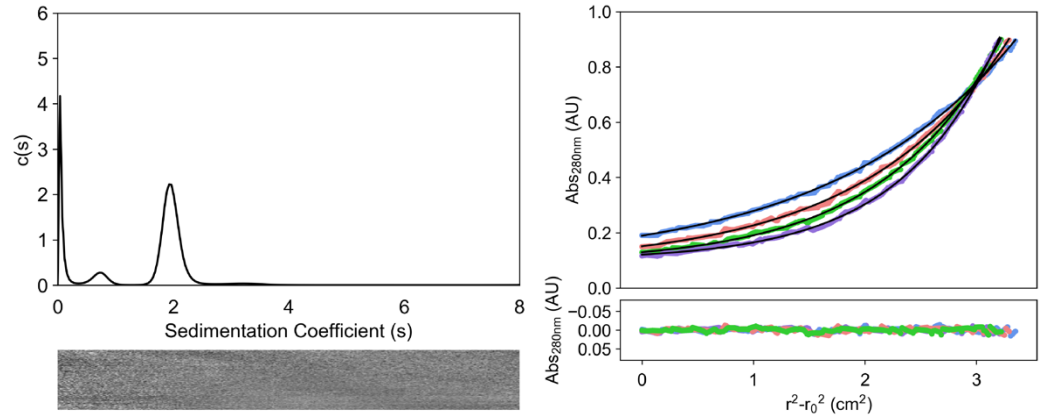


**Figure 34.** AUC data and fits (top) with residuals (bottom) for **CC-Type2-($L_aS_d$)$_5$** ($\bar{\nu}$ = 0.743**)**. Left: sedimentation velocity continuous c(s) distribution at 50 krpm (s = 1.97 S, $s_{20,w}$ = 2.00 S, f/$f_0$ = 1.32, Mw = 19750, 5.1x monomer mass at a 95% confidence level). Conditions: 20 °C, 10 mM Tris-HCl, 100 mM KCl, pH 8. Right: sedimentation equilibrium data and fitted curves from 18 – 36 krpm for a single-species model (Mw = 19100 Da, 4.9x monomer mass, 95% confidence limits 19031 – 19168 Da). Conditions: 20 °C, 10 mM HEPES, 100 mM KCl, pH 7.4. SV and SE experiments were conducted at 150 and 75 μM concentrations, respectively.

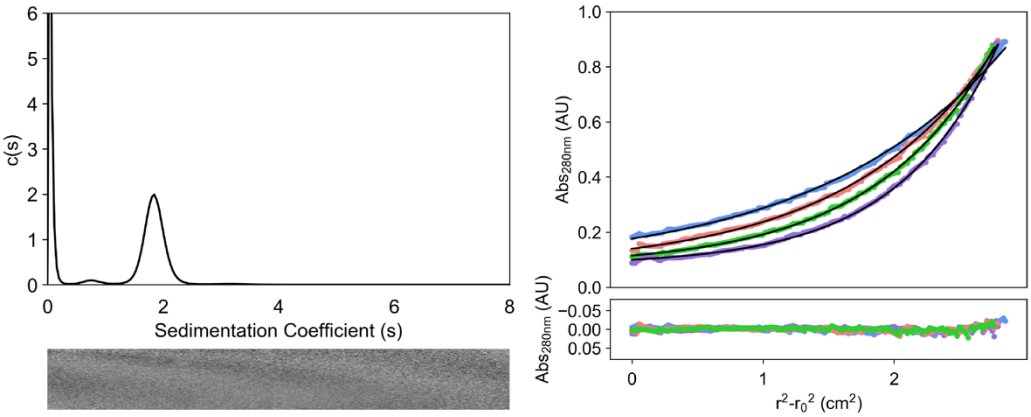


**Figure 35.** AUC data and fits (top) with residuals (bottom) for **CC-Type2-($T_aS_d$)$_2$** ($\bar{\nu}$ = 0.754). Left: sedimentation velocity continuous c(s) distribution at 50 krpm ($f/f_0$ = 1.40, 1.85 S, $s_{20,w}$ = 1.88 S, Mw = 22828 Da, 5.8x monomer mass). Right: sedimentation equilibrium data and fitted curves from 18 – 36 krpm for a single-species model (Mw = 22118, 5.6x monomer mass, 95% confidence limits 22034 – 22203 Da). Conditions: 20 °C, 10 mM Tris-HCl, 100 mM KCl, pH 8. SV and SE experiments were conducted at 150 and 75 µM concentrations, respectively.

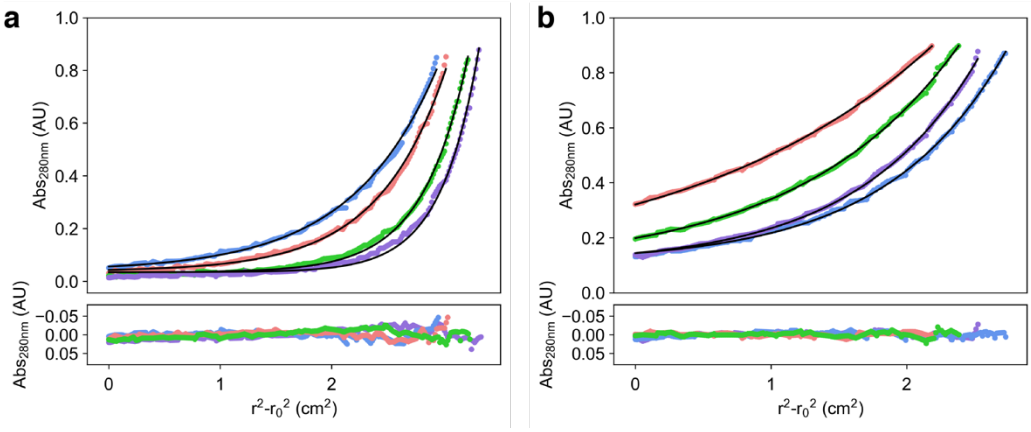


**Figure 36.** AUC sedimentation equilibrium data for **CCTM-$V_bI_c$** in the presence of a) pentaethylene glycol monooctyl ether ($C_8E_5$ ) and b) n-dodecylphosphocholine (DPC). Profiles were fitted to a single-species model. Large systematic errors in the residuals indicate multiple species were likely present in solution. While fitting to multi-component models was attempted, a single suitable and unambiguous model was not be found. a) Mw = 44480 Da, 12.4x monomer mass. Conditions: 20 °C, 37.5 µM peptide concentration, 0.5% $C_8E_5$, 10 mM Tris-HCl, 100 mM KCl, pH 8. b) Mw = 13560 Da, 3.8x monomer mass. Conditions: 20 °C; 19, 38, 56 µM peptide concentrations; 59.5% $D_2O$; 0.35% DPC; 10 mM Tris-HCl; 100 mM KCl; pH 8.

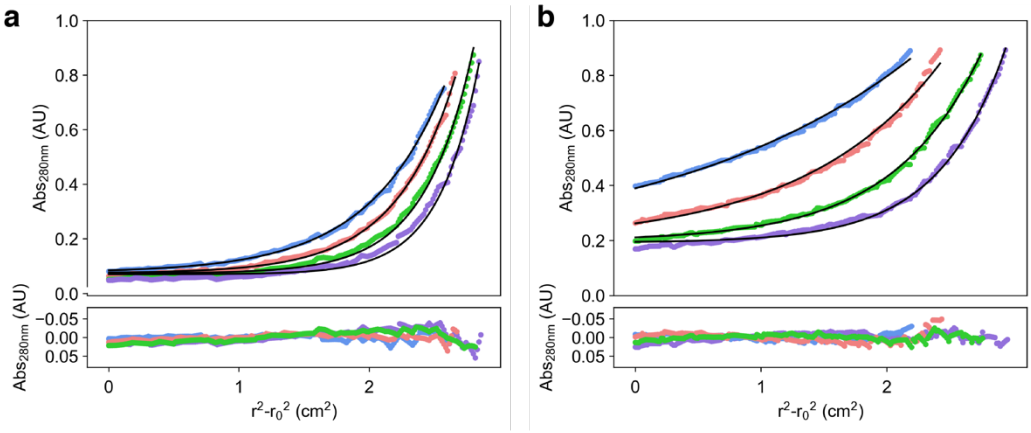


**Figure 37.** AUC sedimentation equilibrium data for **$K_2$-CCTM-$V_bI_c$** in the presence of a) $C_8E_5$ and b) DPC. Profiles were fitted to a single-species model. Large systematic errors in the residuals indicate multiple species were likely present in solution. While fitting to multi-component models was attempted, a single suitable and unambiguous model was not be found. a) Mw = 58200 Da, 18.9x monomer mass. Conditions: 20 °C, 37.5 µM peptide concentration, 0.5% $C_8E_5$, 10 mM Tris-HCl, 100 mM KCl, pH 8. b) Mw = 22400 Da, 7.3x monomer mass. Conditions: 20 °C; 19, 38, 56 µM peptide concentrations; 59.5% $D_2O$; 0.35% DPC; 10 mM Tris-HCl; 100 mM KCl; pH 8.

## DPH binding data

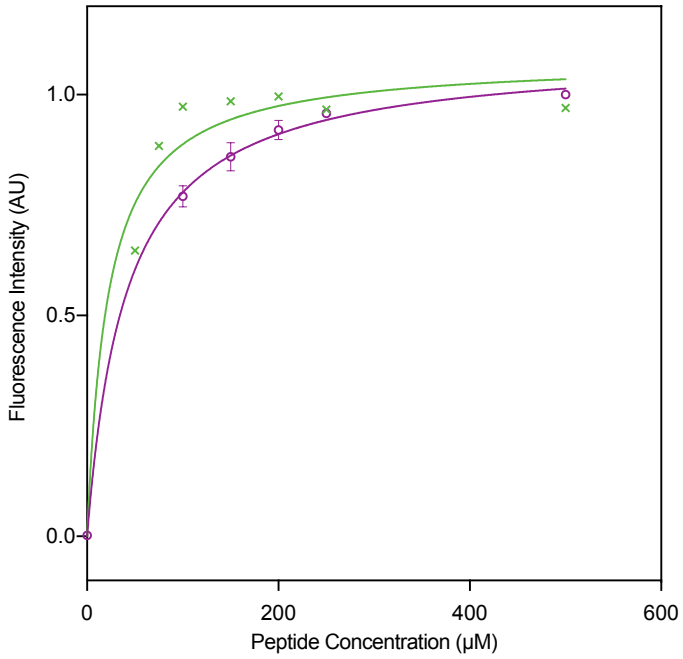


**Figure 38.** Normalized DPH binding plots for **CC-Type2-($T_aI_d$)$_5$** (purple) and **CC-Type2-($T_aS_d$)$_2$** (green). Dots and error bars represent the mean and one standard deviation, respectively, of at least 3 independent measurements. Conditions: 5 % v/v DMSO, 0.1 μM DPH, HEPES 10 mM, KCl 100 mM, pH 7.4. $K_d$ relative to peptide for CC-Type2-($T_aI_d$)$_5$ = 40.8 μM (std. error ± 3.5 μM). $K_d$ relative to peptide for CC-Type2-($T_aS_d$)$_2$ = 21.7 μM (std. error ± 8.42 μM).

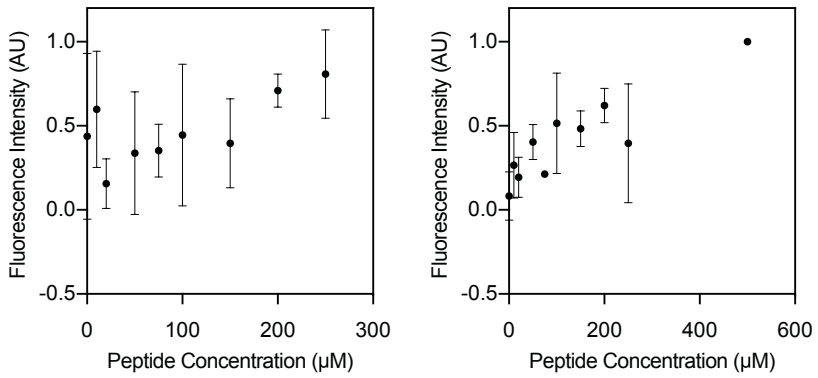


**Figure 39.** Normalized DPH titrations for **CC-Type2-($L_aS_d$)$_5$** (left) and **CC-Type2-($L_aT_d$)$_5$** (right). Conditions: 5 % v/v DMSO, 1 μM DPH, HEPES 10 mM, KCl 100 mM, pH 7.4.

**PHENIX Polder omit map**

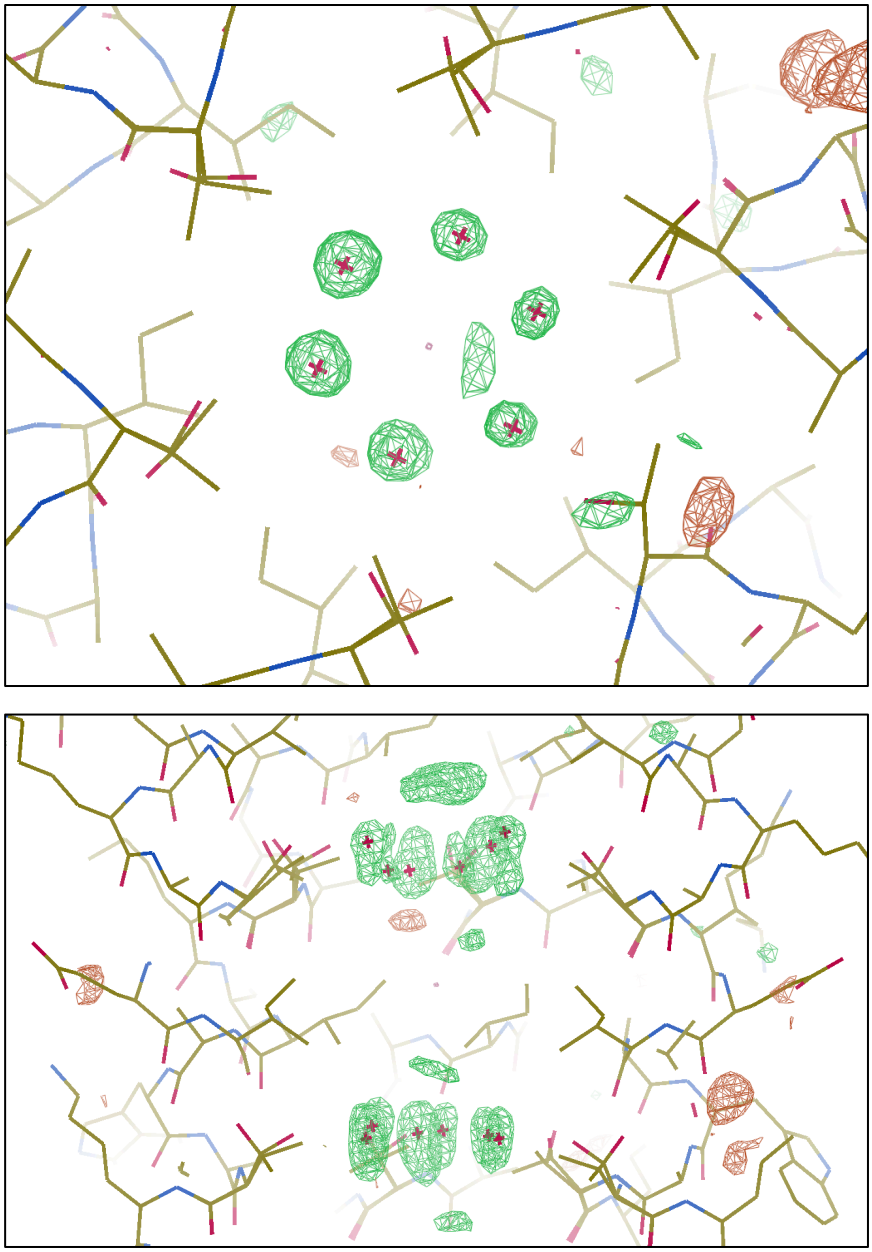

**Figure 40.** PHENIX Polder Omit map[32] from the crystal structure of CC-Type2-$(T_aI_d)_2$, generated by omission of the modelled water molecules and proximal bulk solvent within the Thr layers. Local correlation coefficients: $CC_{1,2} = 0.23$, $CC_{1,3} = 0.76$, $CC_{2,3} = 0.39$. Peak correlation coefficients: $CC_{1,2} = 0.37$, $CC_{1,3} = 0.69$, $CC_{2,3} = 0.44$.

## MD simulation data (water-soluble barrels)

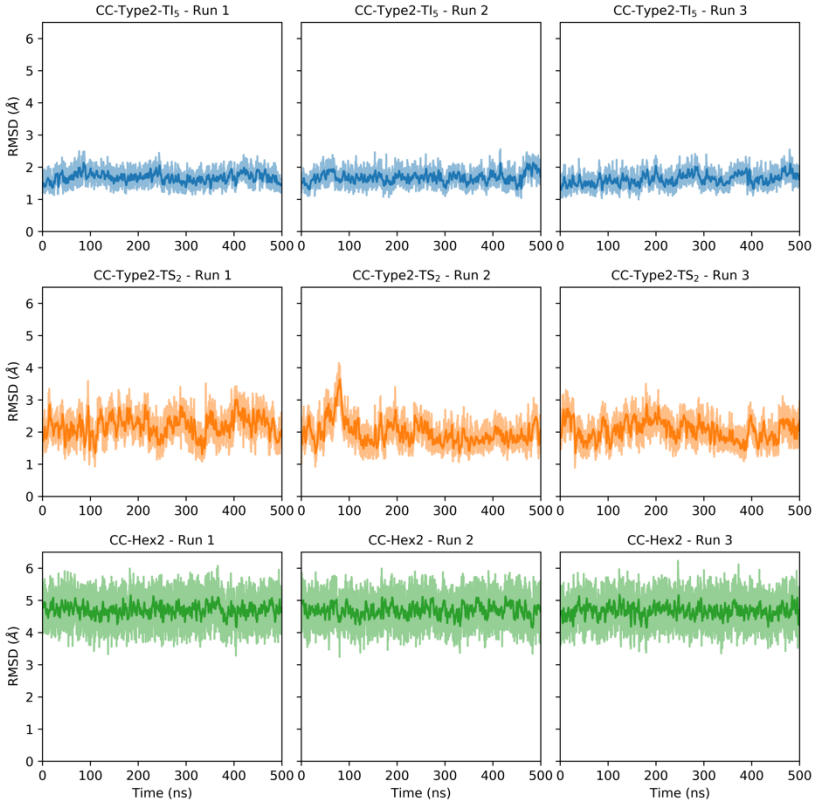


**Figure 41.** Backbone root mean square deviation (RMSD) for each replica production MD simulations for **CC-Type2-($T_aI_d$)$_5$** (top - blue), **CC-Type2-($T_aS_d$)$_2$** (centre – orange) and (**CC-Type2-($L_aI_dS_g$)$_5$** (CC-Hex2; bottom – green) with respect to the crystal structure. The lighter traces correspond to the actual RMSD values, whereas the darker lines are the moving average. Backbone RMSD calculations reveal that the simulated structures are stable over the course of the MD simulations and no major conformational changes are observed at the investigated timescales. As observed previously [5], **CC-Type2-($L_aI_dS_g$)$_5$** deviates significantly from the crystal structure during the MD simulations, due to a straightening of the helices, leading to a longer and narrower channel. However, once this relaxation has occurred (during the MD equilibration phase), the newly adopted conformation remains very stable.

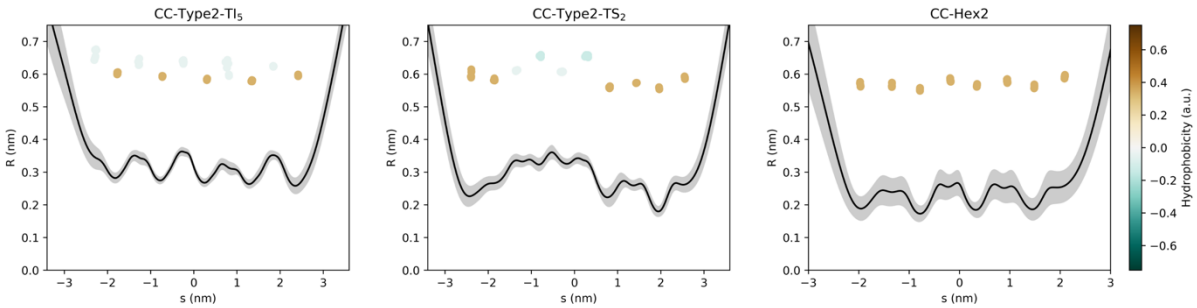


**Figure 42.** Radius of the channels of **CC-Type2-($T_aI_d$)$_5$** (left), **CC-Type2-($T_aS_d$)$_2$** (centre) and **CC-Type2-($L_aI_dS_g$)$_5$** (CC-Hex2, right). The coordinates correspond to the distance along the channel axis oriented from the *C* terminus (left) to the *N* terminus (right) with the origin set to the centres of the barrels. On each graph the average and standard deviation of the channel radius over the course of the MD simulations are represented by a black line and dark grey area, respectively. The coloured circles represent the position of the Cα of the channel lining residues and are coloured based on the residue hydrophobicity, ranging from dark cyan (hydrophilic) to dark brown (hydrophobic). Analysis of the channel radius and volume (Supplementary Figure 43) for **CC-Type2-($T_aI_d$)$_5$**, **CC-Type2-($T_aS_d$)$_2$** and **CC-Type2-**

**(LaIdSg)5** confirm that the channels remain open and do not collapse even if entirely or partly dry (Supplementary Figure 44Figure 45).

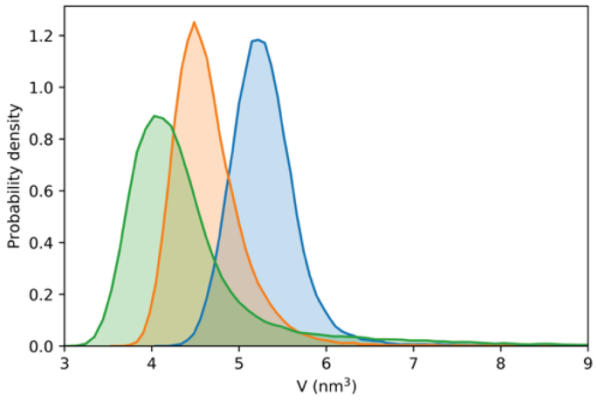


**Figure 43.** Probability density function for the channel volume *V* over the course of the MD simulations for **CC-Type2-(TaId)5** (blue), **CC-Type2-(TaSd)2** (orange) and **CC-Type2-(LaIdSg)5** (green).

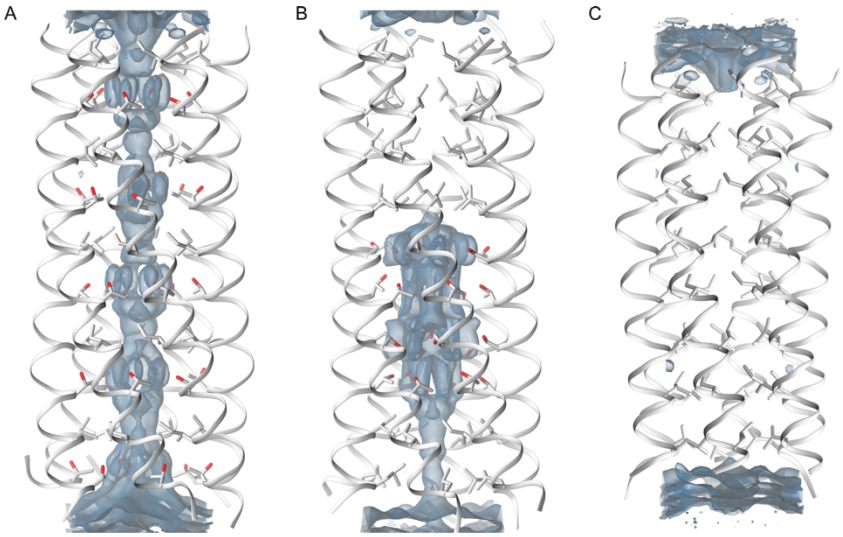


**Figure 44.** Water density map for **CC-Type2-(TaId)5** (A), **CC-Type2-(TaSd)2** (B) and **CC-Type2-(LaIdSg)5** (C). Normalised water density over the course of the MD simulations, contoured at a density level of 0.8 g/L, is shown as a blue transparent surface. Peptides chains are shown as ribbons and channel lining residues are shown as sticks. The αHBs are oriented with the *N* termini of the helices at the top.

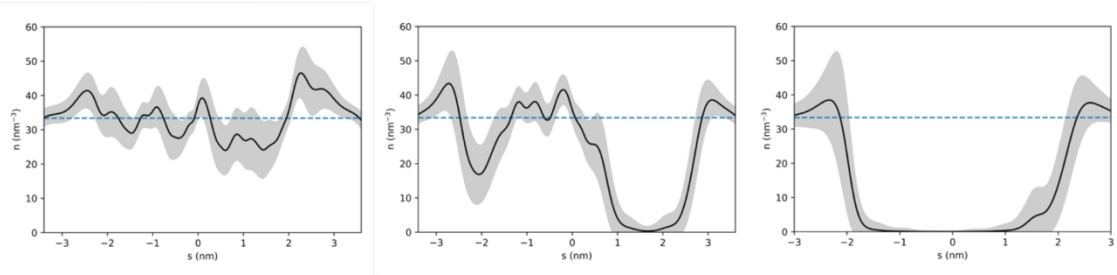


**Figure 45.** Averaged water number density along the channel axis overs the course of the MD simulations. for **CC-Type2-(TaId)5** (left), **CC-Type2-(TaSd)2** (centre) **CC-Type2-(LaIdSg)5** (right). On each graph the average and standard deviation of the channel radius over the course of the MD simulations are represented by a black line and dark grey area respectively. The blue dotted horizontal line indicates the number density of bulk water.

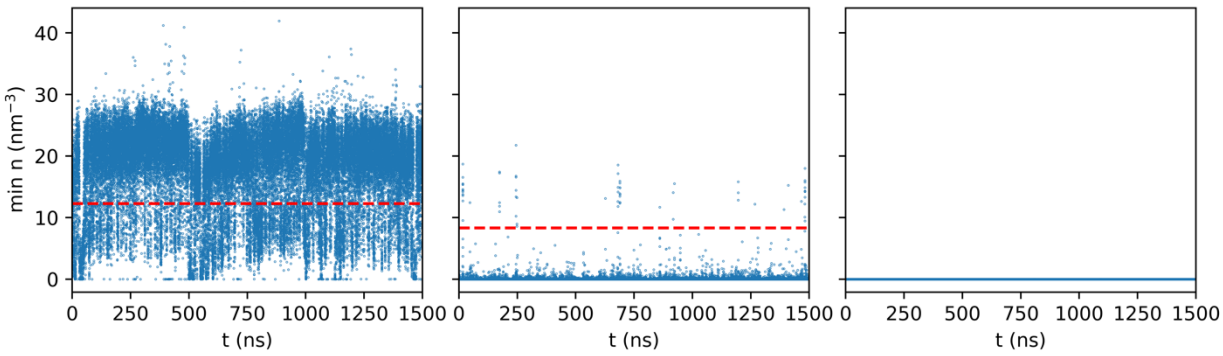


**Figure 46.** Minimum water number density *min n* calculated for each trajectory frames for CC-**Type2-($T_aI_d$)$_5$** (left), **CC-Type2-($T_aS_d$)$_2$** (centre) and **CC-Type2-($L_aI_dS_g$)$_5$** (right). The dotted red lines correspond to the empirically calculated cut-off value for *min n* from which the channel is considered to exhibit a continuous line of water molecules along the channel (see Methods).

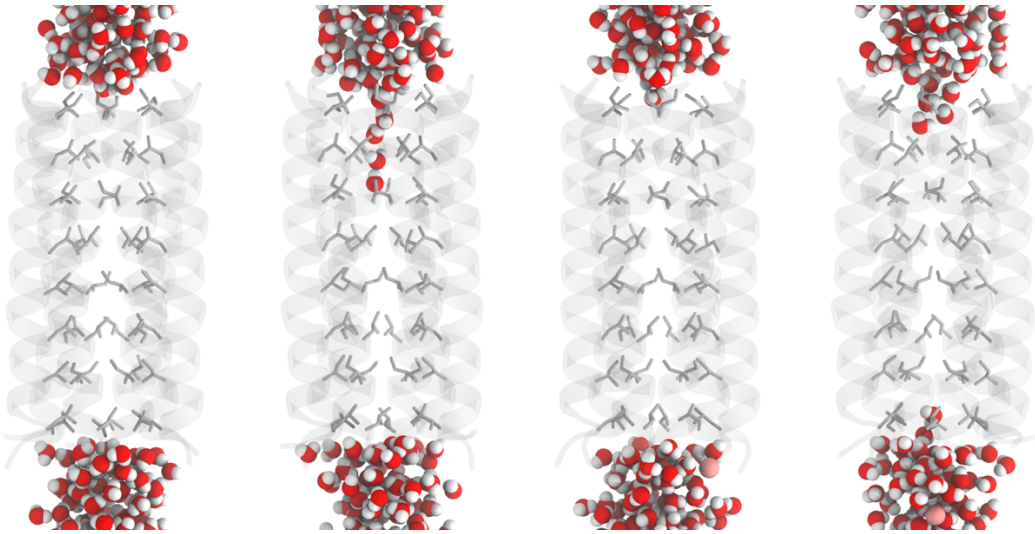

**Figure 47.** Snapshots from the MD simulations of **CC-Type2-($L_aI_dS_g$)$_5$**. The peptide chains are represented with transparent ribbons, pore lining residue side chains with sticks and water molecules and ions as spheres. The αHBs are oriented with the *N* termini of the helices at the top. Apart from the *N*-terminal end of its channel, **CC-Type2-($L_aI_dS_g$)$_5$** is found to be mostly dry (see also Fig. 1, Supplementary Figure 44Figure 45), yet the channel does not collapse (Supplementary Figure 42Figure 43). This is consistent with the concept of hydrophobic gating with water transitioning from a liquid to a vapour state inside the hydrophobic channel (see for example [33-35]). See also Movie 2.

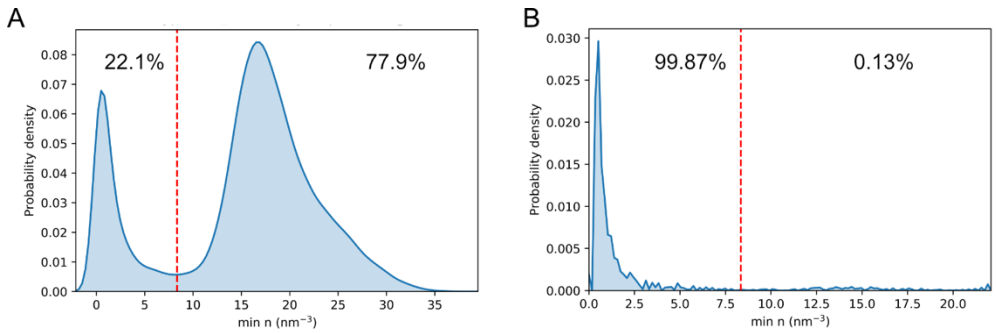


**Figure 48.** Probability density function for the minimum water number density *min n* for **CC-Type2-($T_aI_d$)$_5$** (A) and **CC-Type2-($T_aS_d$)$_2$** (B). The coordinate s corresponds to the distance along the channel axis oriented from the *C* terminus (left) to the *N* terminus (right) with the origin set to the centres of the barrels. The red dotted lines correspond to the empirically calculated cut-off value for *min n* from which the channel is considered to exhibit a continuous line of

water molecules along the channel. The percentages indicated on each side of the red dotted lines correspond to the relative prevalence of each state (continuous or discontinuous chain of water).

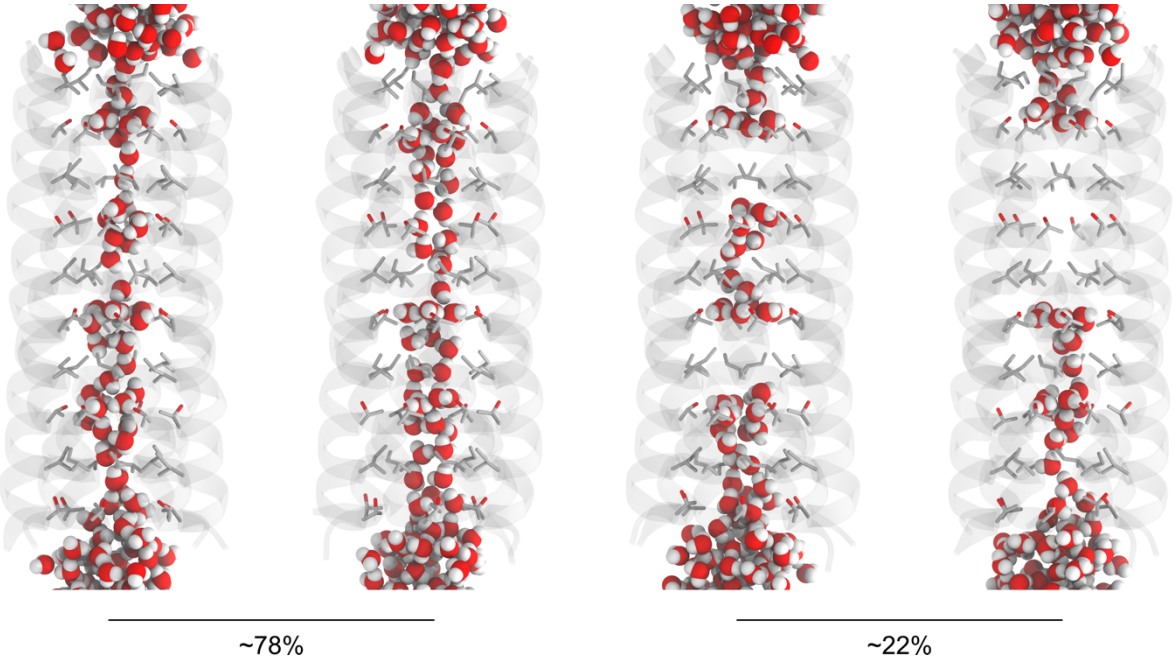


**Figure 49.** Snapshots from the MD simulations of **CC-Type2-($T_aI_d$)$_5$**. The peptide chains are represented with transparent ribbons, pore lining residue side chains with sticks and water molecules and ions as spheres. The αHBs are oriented with the *N* termini of the helices at the top. The percentages below the structures indicate the relative prevalence of the continuous (right) and discontinuous (left) presence of water inside the channel. The channel of **CC-Type2-($T_aI_d$)$_5$** is found to be hydrated (see also Figure 1, Supplementary Figure 44Figure 45). A continuous line of water molecules between the two entrances of the channel is observed in ≈78% of the trajectory frames (see Supplementary Figure 50). Discontinuity in the water chain along the channel is explained by the dewetting of one or more hydrophobic sections sometimes accompanied by the dewetting of an intermediate hydrophilic section. See also Movie 1.

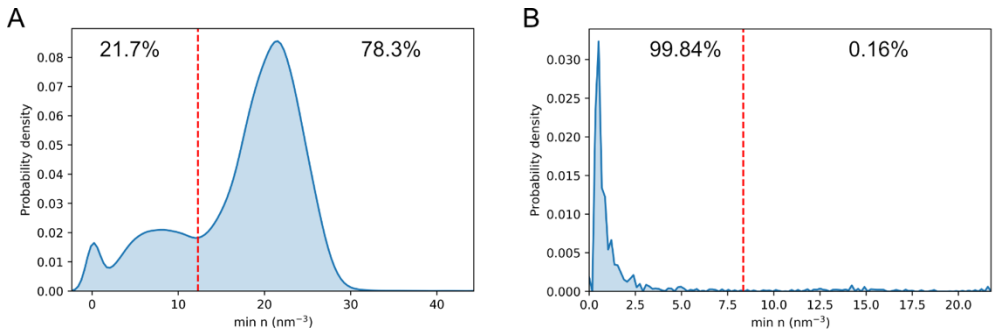


**Figure 50.** Probability density function for the minimum water number density *min n* for the short (A) and long (B) hydrophobic section of the channel of **CC-Type2-($T_aS_d$)$_2$**. The coordinate s corresponds to the distance along the channel axis oriented from the *C* terminus (left) to the *N* terminus (right) with the origin set to the centre of the barrel. The red lines correspond to the empirically calculated cut-off value for *min n* from which the channel is considered to exhibit a continuous line of water molecules along the channel. The percentages indicated on each side of the red dotted lines correspond to the relative prevalence of each state (continuous or discontinuous chain of water). The short hydrophobic section is defined as $-3.0\ nm < s < -1.5\ nm$ and the long as $0.5\ nm < s < 3\ nm$.

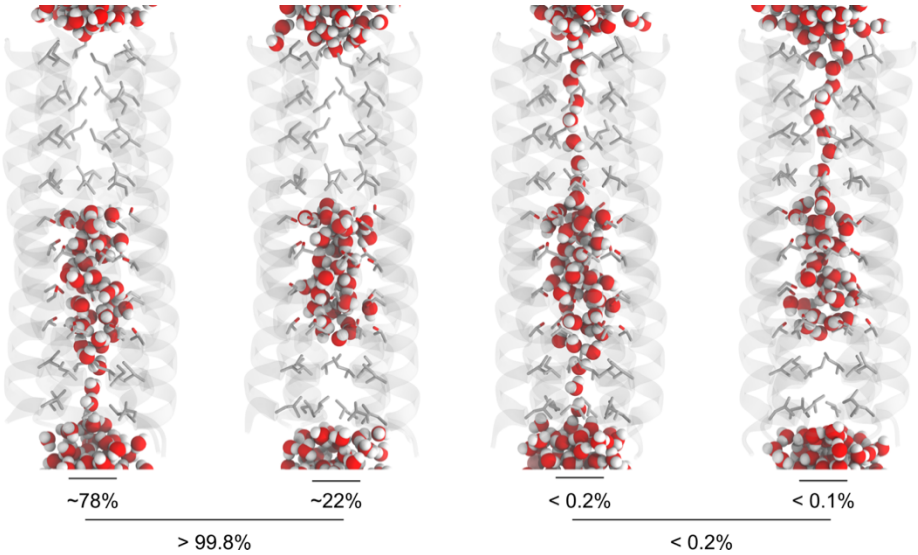


**Figure 51.** Snapshots from the MD simulations of **CC-Type2-($T_aS_d$)$_2$**. The peptide chains are represented with transparent ribbons, pore lining residue side chains with sticks and water molecules and ions as spheres. The αHBs are oriented with the *N* termini of the helices at the top. The percentages below the structures indicates the relative prevalence of the continuous and discontinuous presence of water along the long and short hydrophobic section of the channel. In the case of CC-Type2-($T_aS_d$)$_2$, the radius of the hydrophilic region is larger than that of CC-Type2-($T_aI_d$)$_5$ (Supplementary Figure 42) creating a large water reservoir (section of the channel for which *-1.5 nm* $\leq s \leq$ *0.5 nm)* lined up with Thr and Ser side chains (Supplementary Figure 44). This reservoir is connected to bulk water via the short hydrophobic region at the N-terminal end (*-3.0 nm* $< s <$ *-1.5 nm*) around 78% of the time (see also Supplementary Figure 50A) and very rarely (less than 2‰ of the time – Supplementary Figure 50B) via the long hydrophobic region at the *C* terminal end (*0.5 nm* $< s <$ *3 nm*). Because of this long hydrophobic section, a continuous line of water molecules seldomly connect the two entrances of the channel. See also Movie 3.

## Additional electrophysiology data

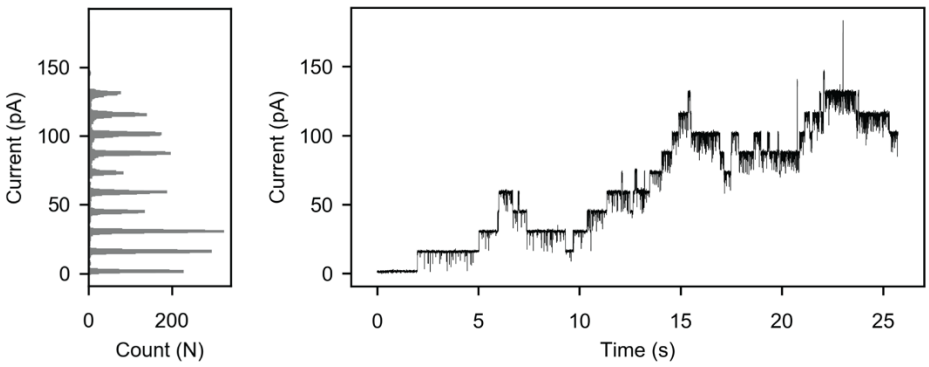


**Figure 52.** Monodisperse and stepwise insertions of **CCTM-$V_bI_c$** at +100 mV. Gating events are evident. Buffer: 10 mM Tris-HCl, pH 8.0. Current signal recorded at 10 kHz and low-pass filtered at 2 kHz.

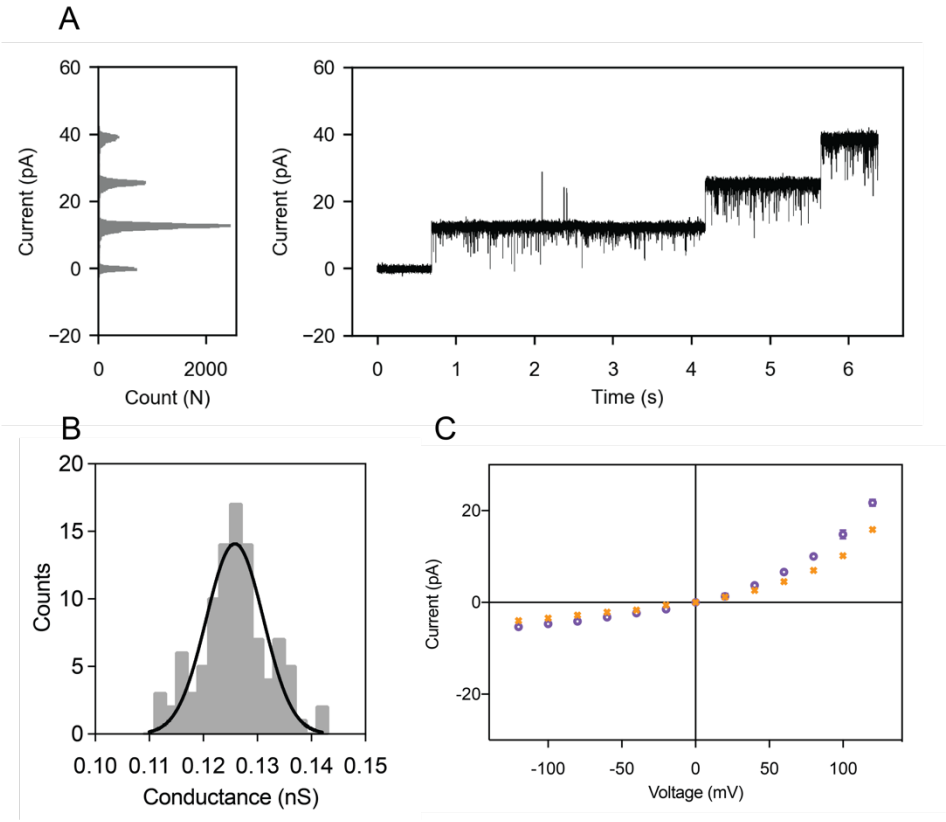


**Figure 53.** A) Monodisperse and stepwise insertions of **$K_2$-CCTM-$V_bI_c$** at +100 mV. Buffer: 10 mM Tris-HCl, pH 8.0. Current signal recorded at 10 kHz and low-pass filtered at 2 kHz. B) Frequency distributions with fitted Gaussian for the conductance of single $K_2$-CCTM-$V_bI_c$ pores (n = 100, $\mu$ = 0.13 nS, $\sigma$ = 0.01 nS) at +100 mV with 1 M KCl. C) Current-voltage curves for single **$K_2$-CCTM-$V_bI_c$**. Electrolyte: 1 M KCl (purple) or NaCl (orange). Buffer: 10 mM Tris-HCl, pH 8.0. All current signals above were recorded at 10 kHz and low-pass filtered at 2 kHz.

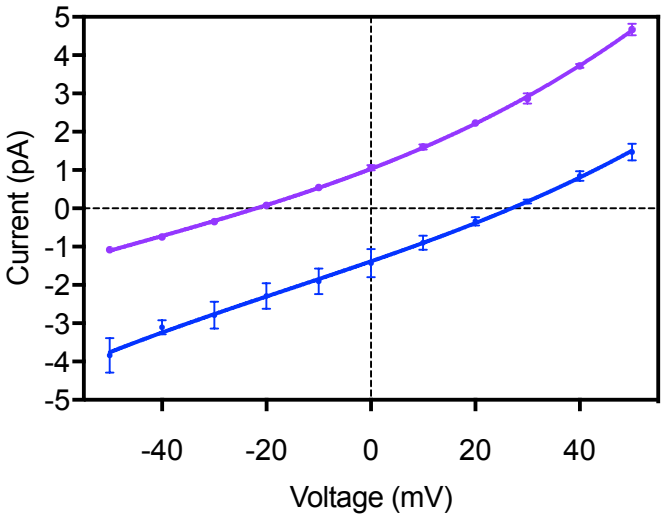


**Figure 54.** Reversal potential measurements for **CCTM-$V_bI_c$**. Purple: 0.2 M KCl *cis*, 1 M KCl *trans* (x-intercept = -22.0 mV, $P_{K+}$ / $P_{Cl-}$ = 4.21). Blue: 1 M KCl *cis*, 0.2 M KCl *trans* (x-intercept +26.9 mV, $P_{K+}$ / $P_{Cl-}$ = 6.44). Average $P_{K+}$ / $P_{Cl-}$ = 5.33. Buffer: 10 mM Tris-HCl, pH 8.

## Additional oSCR data

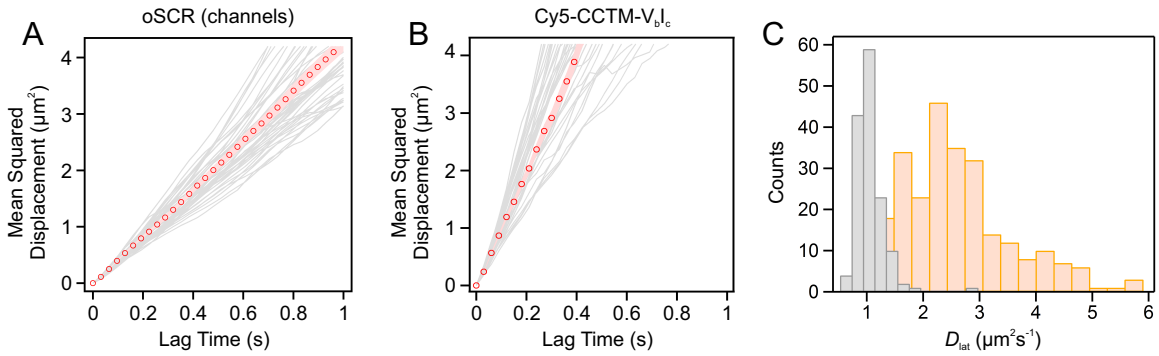


**Figure 55.** MSD vs. *t* analysis. A) Mean-squared displacement versus time plots for **CCTM-$V_bI_c$** channels in DIBs, derived from tracking isolated oSCR signals. 46 curves are shown in grey, with one highlighted in red. Standard deviations of the MSD values are represented by the pink shaded region. The gradient of the curve is equal to $4D_{lat}$; the mean lateral diffusion coefficient ($D_{lat}$) was 1.05 ± 0.26 μm$^2$s$^{-1}$ (n = 143). B) MSD vs. t for Cy5-labelled **CCTM-$V_bI_c$** in the same system; the axes are scaled the same as in A) to highlight the increased rate of diffusion. Mean $D_{lat}$ was 2.56 ± 0.99 μm$^2$s$^{-1}$ (n = 262). C) Histograms of the computed lateral diffusion coefficients for the $Ca^{2+}$-conducting channels (grey, n = 143) and the labelled peptides (orange, n = 262). For details of particle radii estimates see Materials and Methods.

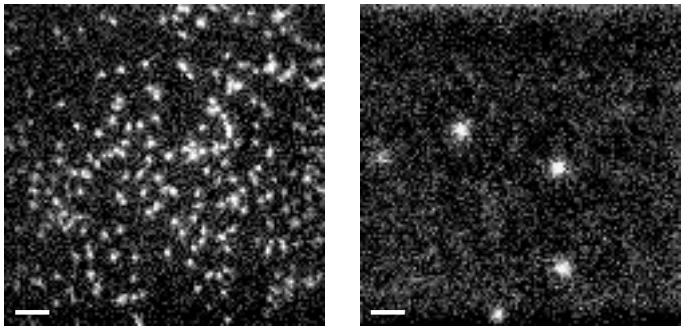

**Figure 56.** Relative surface densities of oSCR signals and labelled **CCTM-$V_bI_c$**. Representative images showing the relative surface densities of Cyanine 5 (Cy5) **CCTM-$V_bI_c$** (left) and the oSCR signal (right) in the same DIB, demonstrating that the peptide carpets the membrane. In the recording from which the oSCR image was extracted, there were at most 6 visible channels. Scale bars: 5 μm.

## MD simulation data ($K_2$-CCTM-$V_bI_c$)

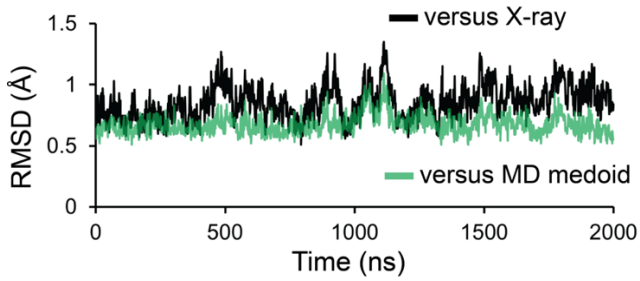


**Figure 57.** Backbone atoms RMSD with respect to **$K_2$-CCTM-$V_bI_c$** crystal structure (black) and a medoid representative conformation obtained after clustering (green) for a 2 μs unrestrained MD simulation of **$K_2$-CCTM-$V_bI_c$** inserted in DPhPC. The mean and maximum RMSD to X-ray structure are 0.9 and 1.4 Å, respectively. The mean and maximum RMSD to the medoid frame structure are 0.7 Å and 1.1 Å, respectively.

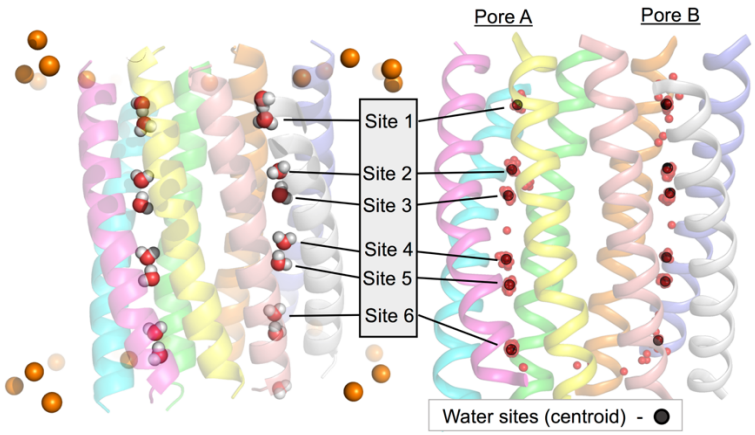


**Figure 58.** Representative frame of **$K_2$-CCTM-$V_bI_c$** MD simulations (**left**) showing the partially hydrated polar interior of the outer tetramers and resident water sites that overlay very well with the ordered waters in the X-ray crystal structure. The orange spheres indicate the position of the lipid phosphates. We identified the 6 innermost sites (**right**) for each interior that can host very stable interactions with water via hydrogen bonding with Ser and Thr side chains (see Methods and Supplementary Figure 59). The centroid position of each of these 12 water sites is represented with black transparent spheres and the water oxygen atom positions from 20 simulation frames are shown as red spheres, illustrating the prevalence of water molecules within these sites. Although water frequently and rapidly exchanged from the defined water sites (Supplementary Figure 60), only very few unique waters ever reach each individual water site (Supplementary Table 5). A given water can bind and unbind extensively to effectively occupy each site over a long period of time (Supplementary Table 5), although those water deviate outside of the 2 Å sphere that we designated from a water site's cluster centroid (see also Methods). Sites 2 and 3 as well as sites 4 and 5 are entirely located in the Ser-Thr region and are ~3.2 Å apart, facilitating the exchange of water between them. In contrast, sites 1 and 2, sites 3 and 4, as well as sites 5 and 6 are ~7 Å apart and separated by a hydrophobic region lined by Ala side chains. Nonetheless, water molecules are found transiently transitioning between these distant sites.

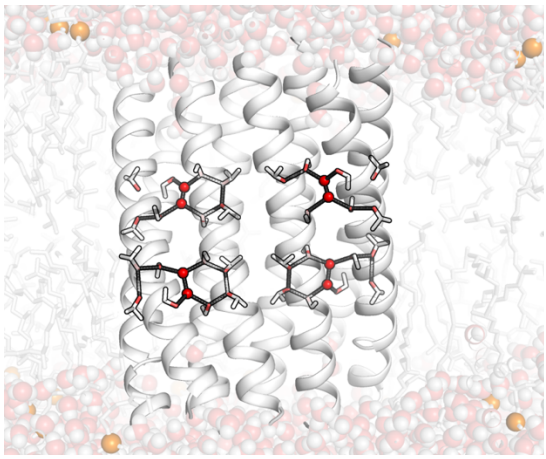

**Figure 59.** Water molecules within the 8 deepest water sites (oxygen atoms as red spheres) are highly stable and maintained by an extensive hydrogen bonded networks with serine and threonine sidechains (black lines).

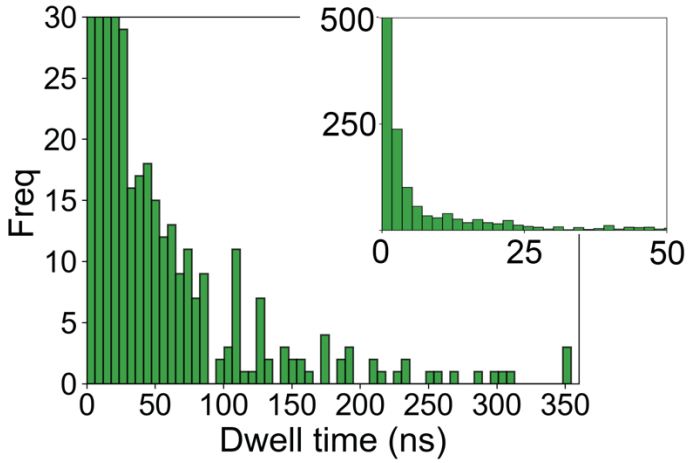


**Figure 60.** Histogram of consecutive dwell times of water for all 12 water sites (Supplementary Figure 57) tracked across the 2 μs **$K_2$-CCTM-$V_bI_c$** simulation. The inset histogram, a zoom-out of the main plot, shows the vast majority of dwell times are very short, <5 ns, constituting more than 50% the water binding events. Yet, a substantial number of very long dwell times are also observed from 5 ns to 354 ns, suggesting waters can form very stable and persistent interactions at these water sites within the protein polar pore (Supplementary Figure 58).

## Electrostatic calculation data

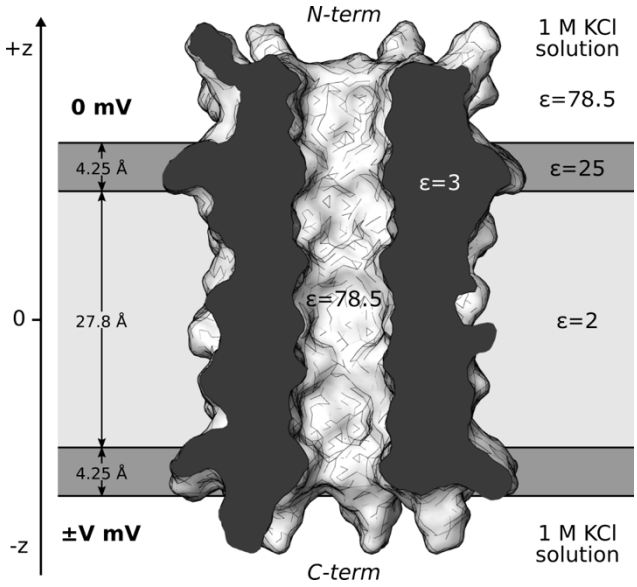


**Figure 61.** Schematic representation of parameters used for electrostatics calculations and modelling of the I-V curves. A parallel hexameric model of **$K_2$-CCTM-$V_bI_c$** is represented in a cut away view, the hydrophobic region of the membrane is coloured in light grey and the polar head group in dark grey. The potential is applied outside of the membrane at z < 0. The *C*-termini of the peptide helices are on the z < 0 side of the membrane.

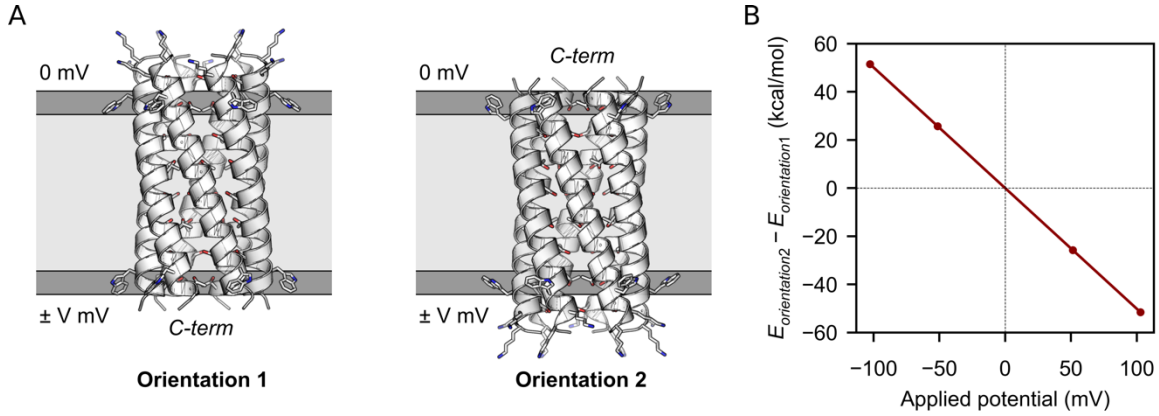


**Figure 62.** Determination of the preferred orientation for the parallel hexamer model of **$K_2$-CCTM-$V_bI_c$** in the presence of a membrane potential. Because the peptide is inserted in the membrane in the presence of a positive potential and each helix as two positively charged Lys residues on their *N* terminus, the orientation of the peptide in the membrane should reflect the preference for the *C*-terminal end to be on the side the potential is applied. To verify this, PB calculations were run with APBSmem to determine the membrane potential contribution to the energy difference between two possible orientations of the peptide: either the *C* termini (Orientation 1) or *N* termini (Orientation 2) of the helices of the on the side of the membrane to which the potential is applied (A). The energy difference between the two orientation ($\Delta \boldsymbol{E} = \boldsymbol{E}_{\boldsymbol{orientation\,2}} - \boldsymbol{E}_{\boldsymbol{orientation\,1}}$), which arises from the interaction of the protein charges with the applied potential, was calculated with the z > 0 side of the membrane was maintained at 0 mV while the z < 0 side was varied from -100 to +100 mV (B). Results indicate that, as expected, Orientation 1 is strongly favoured under a positive potential. Because experimentally the peptides are added in the *cis* side of the membrane while the positive voltage is applied to the *trans* side, the Lys do not have to cross the lipid bilayer, further facilitating insertion of the peptides with the *C* termini on the *trans* side.

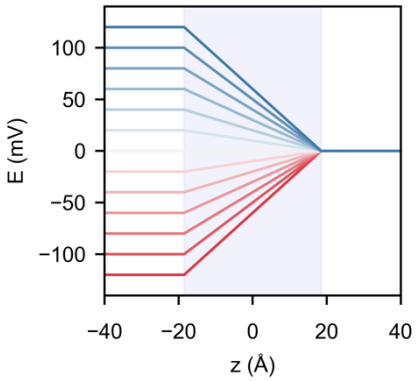


**Figure 63.** Graphical representation of the transmembrane potential $\boldsymbol{\mathcal{V}(z)}$ defined in Eq. 3. A potential, ranging from -120 mV (red) to +120 mV (blue), is applied on the z < 0 side of the membrane. It remains constant in solution but potential drops linearly along the membrane to reach 0 mV on the other side and remains null in solution.

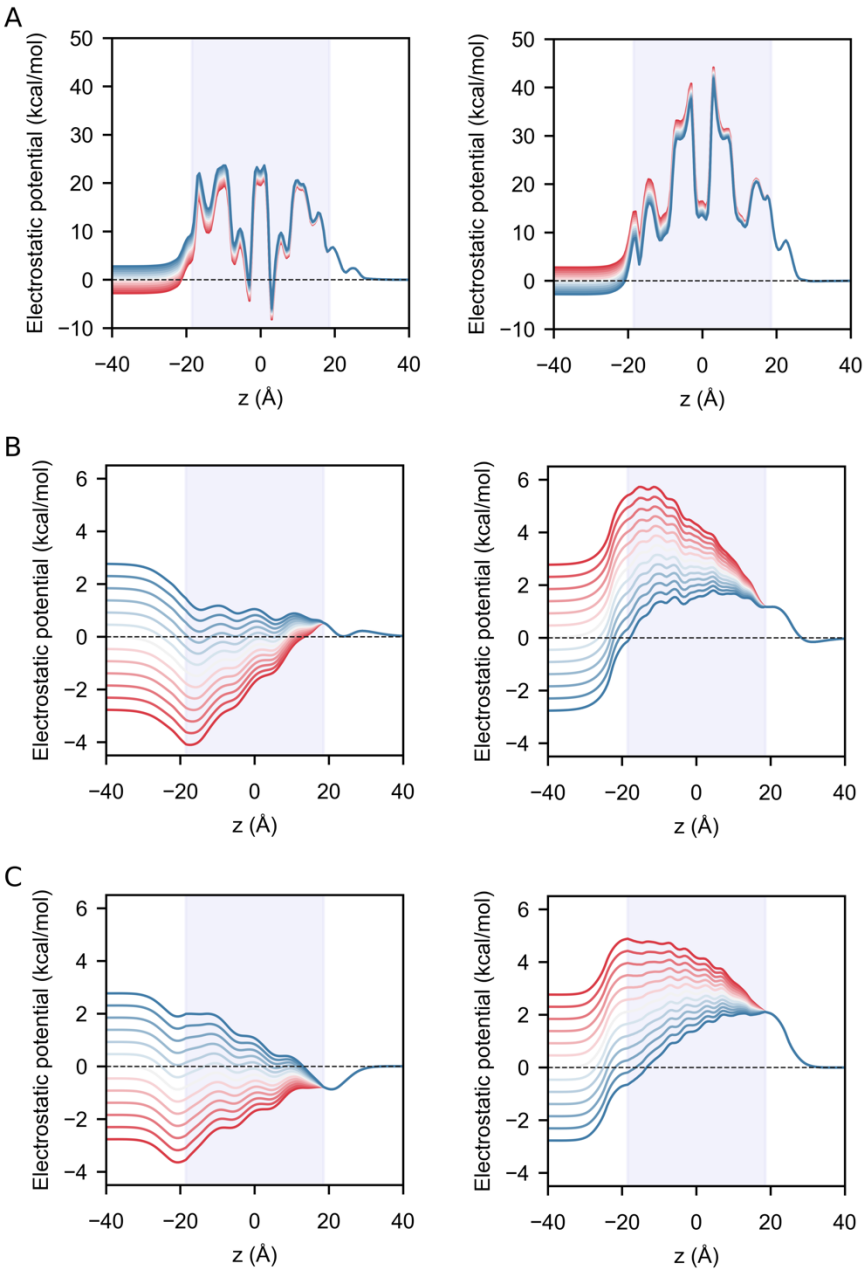


**Figure 64.** Effect of the transmembrane potential $\boldsymbol{\nu(z)}$ defined in Eq. 3 on the electrostatic energy profiles of $K^+$ (left) and $Cl^-$ (right) for the outer four-helix bundle (A), the parallel (B) and anti-parallel (C) models of the hexamer. Plots show the effect for a potential, ranging from -120 mV (red) to +120 mV (blue) by steps of 20 mV applied on the $z < 0$ side of the membrane.

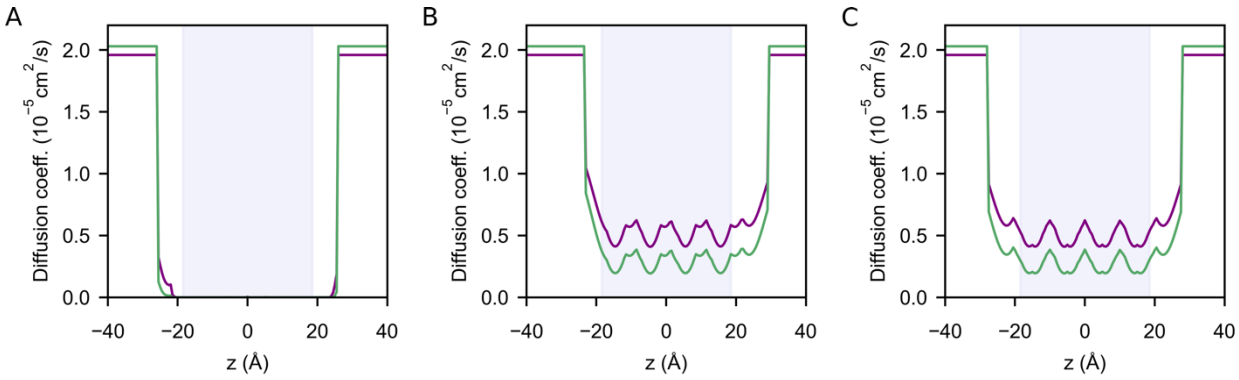


**Figure 65.** Calculated z-dependent diffusion coefficient of $K^+$ (purple) and $Cl^-$ (green) for the outer four-helix bundle (A), the parallel (B) and anti-parallel (C) models of the hexamer. Because the outer four-helix bundle has such a narrow channel, the diffusion coefficients inside the channel is predicted to be close to 0.

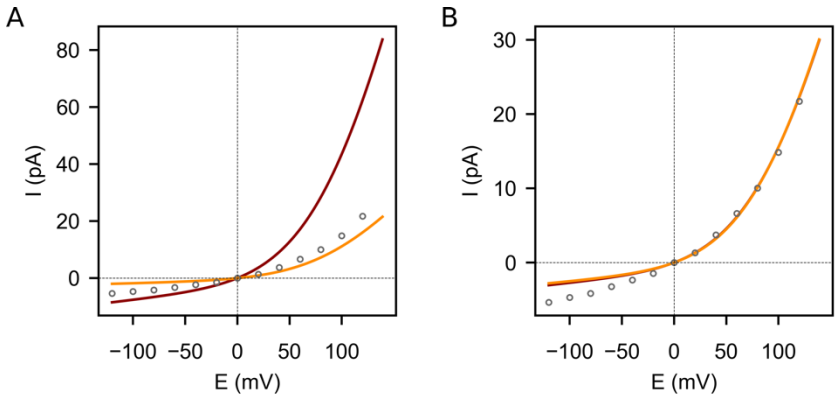


**Figure 66.** Effect of changing the diffusion coefficients. I-V curves were calculated for when Eq. 1 is solved using bulk diffusion coefficients for the ions with a mean value for the channel radius (dark red curve) and using the z-dependent diffusion coefficient calculated in Eq. 5 with a z-dependent channel radius (orange curve) without (A) and with (B) fitting to experimental data using Eq. 6. The fitting coefficient is equal to 0.36 and 1.40 for the bulk and the z-dependent diffusion coefficients respectively. Experimental data are shown as points. From these plots it can be seen that employing z-dependent diffusion coefficients led to predicted currents that deviate less from experimental data in the absence of fitting. However, upon fitting the two methods lead essentially to the same model. Because the fitting coefficient is smaller when using the z-dependent diffusion coefficients, we used this approach in all the calculations.

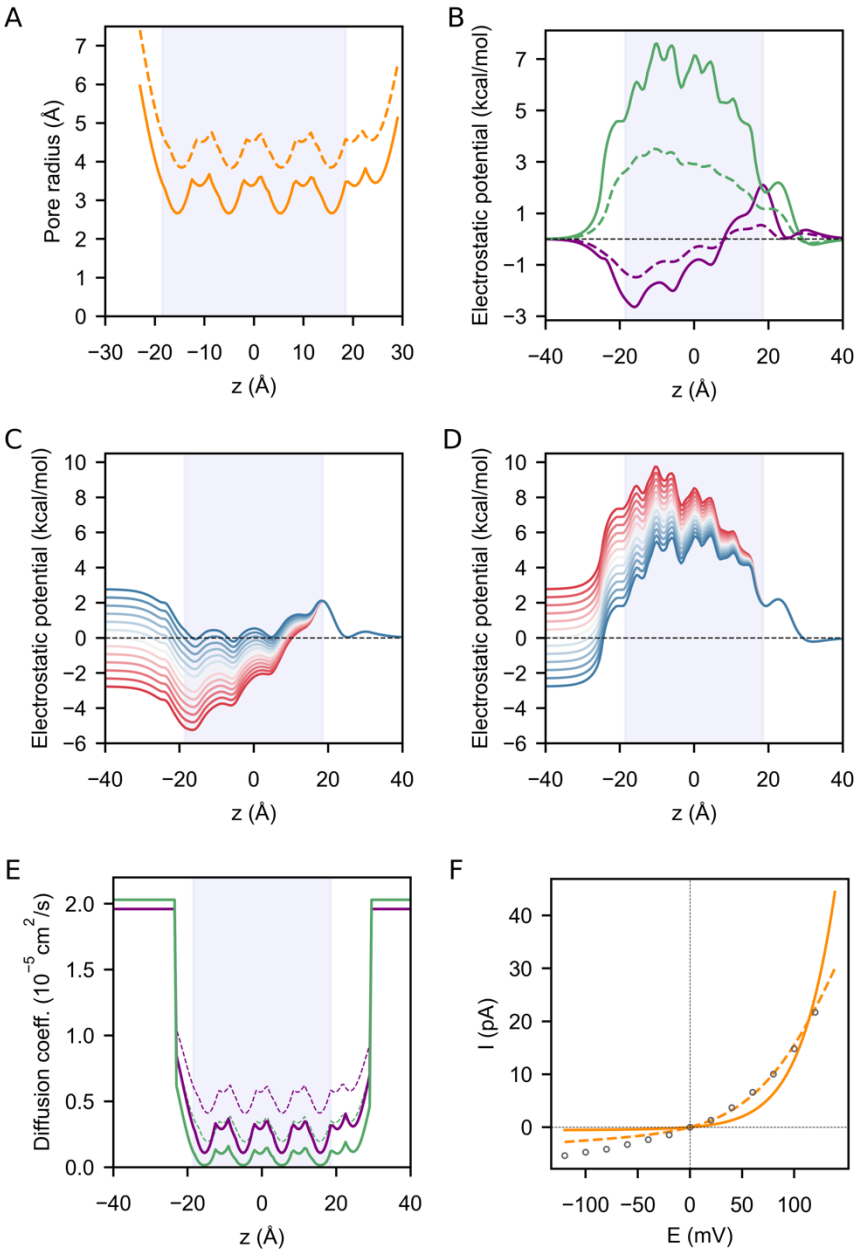


**Figure 67.** Effect of changing the channel radius of the parallel hexamer on the calculated I-V curves. Because the radius of the channel has significant indirect and direct effects when solving both the PB and NP equations, we decided to test the robustness of our predictions by preparing a second model of the parallel hexamer but instead of using the X-ray parameters of **CC-Type2-($T_aS_d$)$_2$** (X-ray parameters), we optimized the model in CCBuilder 2.0 (optimization parameters), yielding a parallel hexamer with a narrower channel. The model generated using the optimization parameters is represented as plain lines whereas the model generated with the X-ray parameters is represented as dotted lines. A) Channel radius calculated with HOLE. B) Electrostatic energy profile for $Cl^-$ (green) and $K^+$ (purple) displacement along the channel axis. C) Effect of an applied potential ranging from -120 mV (red) to +120 mV (blue) on the electrostatic energy profile of $K^+$ along the channel. D) As (C) but for $Cl^-$. E) Profile of the diffusion coefficients for $Cl^-$ (green) and $K^+$ (purple) along the channel axis. F) Calculated I-V curves after fitting using Eq. 6 (c = 7.90 and 1.40 for the model generated with the optimization parameters and the X-ray parameters, respectively), with experimental data shown as points. Because the channel is narrower (A), the energy profile of ion translocation along the channel shows higher barriers and lower energy wells (B), especially in the presence of a negative applied potential (C&D). Because of the narrower channel the diffusion coefficients are significantly lower than for the model generated with X-ray parameters with the diffusion of $Cl^-$ becoming very small in the narrowest section of the channel. Yet the trend of the I-V curve calculated for the model generated with the optimization parameters is similar to that of the

model generated with the X-ray parameters (F), albeit with a larger fitting coefficient (i.e. smaller calculated currents) and a more pronounced rectification.

## Data tables

**Table 1.** Complete table of peptides synthesised.

| Name | Full Sequence |
|---|---|
| **CC-Type2-$(T_aI_d)_2$** | Ac-G EIAQALK EIAKATK EIAWATK EIAQALK G-$NH_2$ |
| **CC-Type2-$(L_aT_d)_2$** | Ac-G EIAQALK ETAKALK ETAWALK EIAQALK G-$NH_2$ |
| **CC-Type2-$(T_aI_d)_5$** | Ac-G EIAQATK EIAQATK EIAKATK EIAWATK EIAQATK G-$NH_2$ |
| **CC-Type2-$(L_aT_d)_5$** | Ac-G ETAQALK ETAQALK ETAKALK ETAWALK ETAQALK G-$NH_2$ |
| **CC-Type2-$(S_aI_d)_5$** | Ac-G EIAQASK EIAQALK EIAKASK EIAWASK EIAQASK G-$NH_2$ |
| **CC-Type2-$(L_aS_d)_5$** | Ac-G ESAQALK ESAQALK ESAKALK ESAWALK ESAQALK G-$NH_2$ |
| **CC-Type2-$(L_aN_d)_5$** | Ac-G ENAQALK ENAQALK ENAKALK ENAWALK ENAQALK G-$NH_2$ |
| **CC-Type2-$(L_aQ_d)_5$** | Ac-G EQAQALK EQAQALK EQAKALK EQAWALK EQAQALK G-$NH_2$ |
| **CC-Type2-$(T_aS_d)_2$** | Ac-G EIAQALK EIAQALK ESAKATK ESAWATK EIAQALK G-$NH_2$ |
| **CC-Type2-$(T_aS_d)_3$** | Ac-G EIAQALK ESAQATK ESAKATK ESAWATK EIAQALK G-$NH_2$ |
| **CCTM-$L_bL_c$** | Ac-KKKKGSG ISAWATL LSALATL LSALATL LSAWATL G-$NH_2$ |
| **CCTM-$V_bI_c$** | Ac-KKKKGSG ISAWATV ISALATV ISALATV ISAWATV G-$NH_2$ |
| **Cy5-CCTM-$V_bI_c$** | Cy5-KKKKGSG ISAWATV ISALATV ISALATV ISAWATV G-$NH_2$ |
| **$K_2$-CCTM-$V_bI_c$** | Ac-G KKSAWATV ISALATV ISALATV ISAWATV G-$NH_2$ |
| **CCTM-$I_bI_c$** | Ac-KKKKGSG ISAWATI ISALATI ISALATI ISAWATI G-$NH_2$ |
| **CCTM-$I_bL_c$** | Ac-KKKKGSG ISAWATL ISALATL ISALATL ISAWATL G-$NH_2$ |

**Table 2.** Crystallographic data collection statistics and model refinement statistics. Highest resolution shell shown in parenthesis. $R_{free}$ represents the *R*-factor calculated from reflections that were not used in refinement (5% of total).

| | **CC-Type2-$(T_aI_d)_2$ PDB code: 6YB2** | **CC-Type2-$(T_aI_d)_5$ PDB code: 6YAZ** | **CC-Type2-$(T_aS_d)_2$ PDB code: 6YB0** | **$K_2$-CCTM-$V_bI_c$ PDB code: 6YB1** |
|---|---|---|---|---|
| **Data Collection** | | | | |
| Wavelength (Å) | 0.94999 | 0.97950 | 0.91974 | 1.11582 |
| Space Group | P $2_1$ $2_1$ $2_1$ | P 1 | P $2_1$ $2_1$ $2_1$ | P$3_1$12 |
| Unit Cell *a, b, c* (Å) | 31.0, 56.0, 90.6 | 40.1, 43.3, 83.0 | 76.4, 81.6, 90.6 | 47.9, 47.9,103.2 |
| Unit Cell $\alpha$, $\beta$, $\gamma$ (°) | 90, 90, 90 | 102, 97.7, 90.2 | 90, 90, 90 | 90, 90, 120 |
| Resolution (Å) | 23.8 – 1.18 (1.20 – 1.18) | 40.29 – 1.94 (1.97 – 1.94) | 81.6 – 1.86 (1.89 – 1.86) | 26.5 – 2.15 (2.23 – 2.15) |
| Reflections Total | 601090 (21633) | 237647 (6571) | 624649 (28834) | 143376 (9617) |
| Reflections Unique | 52714 (2562) | 39971 (1922) | 48308 (2272) | 7539 (702) |
| Multiplicity | 11.4 (8.4) | 5.9 (3.4) | 12.9 (12.7) | 19.0 (13.7) |
| $R_{merge}$ | 0.071 (1.69) | 0.102 (0.678) | 0.121 (2.37) | 0.099 (1.275) |
| Mean I / σI | 12.8 (1.1) | 7.7 (1.1) | 10.6 (1.07) | 22.10 (1.84) |
| $CC_{1/2}$ | 0.998 (0.631) | 0.993 (0.516) | 0.999 (0.431) | 1.000 (0.809) |
| Completeness (%) | 99.8 (98.8) | 99.2 (94.4) | 99.9 (95.6) | 99.2 (95.3) |
| Wilson B-Factor | 15.4 | 32.2 | 22.0 | 40.6 |
| **Refinement** | | | | |
| Reflections Used | 50029 | 38966 | 48192 | 7525 |
| $R_{work}$ / $R_{free}$ | 0.161 / 0.191 | 0.210 / 0.232 | 0.190 / 0.228 | 0.180 / 0.210 |
| Protein Atoms | 2977 | 3439 | 3270 | 869 |
| Solvent Atoms | 141 | 118 | 296 | 94 |
| Average B-factor | 29.4 | 60.0 | 44.0 | 60.2 |
| RMS (bonds, Å) | 0.008 | 0.015 | 0.012 | 0.004 |
| RMS (angles, °) | 0.88 | 1.49 | 1.28 | 0.61 |
| Clashscore | 12 | 8.37 | 2.96 | 2.04 |

**Table 3.** bZIP scoring for a T*bc*S*efg* Type-2 interface, with positions *b* and *c* restricted to L, I or V. Interface pairs *gade1* and *gade2* correspond to positions *cSgT* and *SeTb*, respectively. Fitness scores for interface pairs were assigned by subtracting the higher Self-Association score for the homo-assembly from Raw score for the desired heteromeric assembly. *N.b.*, bZIP scores are a unitless estimate of coiled-coil pairing energy.

| ***gade*1** | ***gade*2** | **Fitness Score** | **Raw Score** | ***gade*1 Self-Association Score** | ***gade*2 Self-Association Score** |
|---|---|---|---|---|---|
| ISAT | SATV | 28.278 | 24.807 | -3.471 | -18.774 |
| ISAT | SATI | 28.142 | 24.671 | -3.471 | -25.261 |
| LSAT | SATI | 27.598 | 18.551 | -9.047 | -25.261 |
| VSAT | SATV | 27.507 | 19.533 | -7.974 | -18.774 |
| LSAT | SATV | 26.837 | 17.790 | -9.047 | -18.774 |
| VSAT | SATI | 26.347 | 18.373 | -7.974 | -25.261 |
| ISAT | SATL | 25.942 | 22.471 | -3.471 | -14.354 |
| LSAT | SATL | 23.059 | 14.012 | -9.047 | -14.354 |
| VSAT | SATL | 22.286 | 14.312 | -7.974 | -14.354 |

**Table 4.** SOCKET [36] output for the $K_2$-CCTM-$V_bI_c$ octamer (PDB ID: 6YB1). Second outer tetramer omitted.

| **Outer Tetramer** | |
|---|---|
| **Helix** | **A (W)** |
| extent of coiled coil packing | 4- 28:A |
| sequence | KKSAWATVISALATVISALATVISAWATV |
| register | abcdefgabcdefgabcdefgabcd |
| partner | -----XZ!XZ!-XZ!XZ!-XZ!-Z----! |
| knobtype | -----442344-444444-444-4----2 |
| repeats | 0 non-canonical interrupts in 25 residues: 7,7,7,4 |
| **Helix** | **B (X)** |
| extent of coiled coil packing | 4- 28:B |
| sequence | KKSAWATVISALATVISALATVISAWATV |
| register | abcdefgabcdefgabcdefgabcd |
| partner | -----WY-WY--WY-WY--WY--Y----- |
| knobtype | -----44-44--44-34--44--4----- |
| repeats | 0 non-canonical interrupts in 25 residues: 7,7,7,4 |
| **Helix** | **C (Y)** |
| extent of coiled coil packing | 4- 28:C |
| sequence | KKSAWATVISALATVISALATVISAWATV |
| register | abcdefgabcdefgabcdefgabcd |
| partner | -----ZX-ZX--ZX-ZX--ZX--X----- |
| knobtype | -----44-44--44-34--44--4----- |
| repeats | 0 non-canonical interrupts in 25 residues: 7,7,7,4 |
| **Helix** | **D (Z)** |
| extent of coiled coil packing | 4- 28:D |
| sequence | KKSAWATVISALATVISALATVISAWATV |
| register | abcdefgabcdefgabcdefgabcd |
| partner | -----YW!YW!-YW!YW!-YW!-W----- |
| knobtype | -----442344-444444-444-4----- |
| repeats | 0 non-canonical interrupts in 25 residues: 7,7,7,4 |
| **Inner Tetramer** | |
| **Helix** | **A (W)** |
| extent of coiled coil packing | 4- 29:A |
| sequence | KKSAWATVISALATVISALATVISAWATV |
| register | gabcdefgabcdefgabcdefgabcd |
| partner | -----!XZ!XZ-!XZ!XZ-!XZ-X----Z |
| knobtype | -----442344-444444-444-4----2 |
| repeats | 0 non-canonical interrupts in 26 residues: 1,7,7,7,4 |
| **Helix** | **D (X)** |
| extent of coiled coil packing | 4- 29:D |
| sequence | KKSAWATVISALATVISALATVISAWATV |
| register | gabcdefgabcdefgabcdefgabcd |
| partner | -----!WY!WY-!WY!WY-!WY-W----- |
| knobtype | -----442344-444444-444-4----- |
| repeats | 0 non-canonical interrupts in 26 residues: 1,7,7,7,4 |
| **Helix** | **E (Y)** |
| extent of coiled coil packing | 9- 29:E |
| sequence | VISALATVISALATVISAWATV |
| register | efgabcdefgabcdefgabcd |
| partner | X!ZX-!ZX!ZX-!ZX-Z----X |
| knobtype | 2124-444444-444-4----2 |
| repeats | 0 non-canonical interrupts in 21 residues: 3,7,7,4 |
| **Helix** | **H (Z)** |
| extent of coiled coil packing | 4- 26:H |
| sequence | KKSAWATVISALATVISALATVISAWATV |
| register | gabcdefgabcdefgabcdefgabcd |
| partner | -----!YW!YW-!YW!YW-!-W------W |
| knobtype | -----442344-444444-4-4------2 |
| repeats | 0 non-canonical interrupts in 23 residues: 1,7,7,7,1 |

**Table 5.** Analysis of the 8 deepest water binding sites defined in Supplementary Figure 58, and aggregated bound time of unique water molecules in the MD simulation of the **$K_2$-CCTM-$V_bI_c$** octamer. Every site is populated by a water in > 92% of all simulation frames. Waters do not transverse the structure quickly and remain bound at these major water sites for extended period of time. Single unique water molecules may rapidly fluctuate in and out of a specific water site (designated by a 2 Å radius), but the aggregate time spend at each of these sites by a single water molecule is extensive. Each of these sites are only occupied by 5 to 13 unique water molecules. All water sites have a single water molecule that is resident for a total aggregated time of at least 500 ns, with 750.5 ns being the average longest aggregate residency time, and 1015.0 ns being the longest. All sites have at least 4 unique waters that spend >100 ns in aggregate bound.

| Water site | Total occupancy | | Total binding-unbinding events | Events dwelling >45 ns | Unique waters bound | Aggregated bound time of top 3 unique waters | | Transient waters | |
|---|---|---|---|---|---|---|---|---|---|
| | (ns) | (%) | | | | (ns) | (%) | (ns) | (%) |
| 2A | 1997 | 99.8 | 86 | 15 | 10 | 874<br>206<br>204 | 43.7<br>12.5<br>10.3 | 3 | <0.1 |
| 2B | 1841 | 92 | 485 | 10 | 12 | 580<br>385<br>264 | 29<br>19.3<br>13.2 | 3 | <0.1 |
| 3A | 1998 | 99.9 | 61 | 16 | 8 | 583<br>440<br>373 | 29.1<br>22<br>18.6 | 0 | 0 |
| 3B | 1956 | 87.8 | 397 | 11 | 10 | 818<br>762<br>211 | 40.9<br>38.1<br>10.6 | 6 | 0.1 |
| 4A | 1988 | 99.4 | 116 | 14 | 10 | 1015<br>266<br>133 | 50.7<br>13.3<br>6.7 | 2 | 0.1 |
| 4B | 1831 | 91.6 | 65 | 11 | 5 | 648<br>445<br>370 | 32.4<br>22.3<br>18.5 | 1 | <0.1 |
| 5A | 1987 | 99.3 | 277 | 15 | 13 | 537<br>354<br>292 | 26.8<br>17.7<br>14.6 | 5 | <0.1 |
| 5B | 1998 | 98.8 | 137 | 13 | 7 | 805<br>651<br>294 | 40.2<br>32.5<br>14.7 | 2 | <0.1% |

## Movie Captions

**Movie 1.**

500 ns molecular dynamics simulation of **CC-Type2-$(T_aI_d)_5$** showing water ingress into the channel. The peptide chains are represented with transparent ribbons, channel-lining residue side chains with sticks and water molecules and ions as spheres. The αHBs are oriented with the *N* termini of the helices on the left.

**Movie 2.**

500 ns molecular dynamics simulation of **CC-Type2-$(L_aI_dS_g)_4$** showing water ingress into the channel. The peptide chains are represented with transparent ribbons, channel-lining residue side chains with sticks and water molecules and ions as spheres. The αHBs are oriented with the *N* termini of the helices on the left.

**Movie 3.**

500 ns molecular dynamics simulation of **CC-Type2-$(T_aS_d)_2$** showing water ingress into the channel. The peptide chains are represented with transparent ribbons, channel-lining residue side chains with sticks and water molecules and ions as spheres. The αHBs are oriented with the *N* termini of the helices on the left.

**Movie 4.**

oSCR for CCTM-$V_bI_c$ channels in a DPhPC membrane at -60 mV. The field of view is that shown in Fig. 4C.

**Movie 5.**

700 ns molecular dynamics simulation of octameric **$K_2$-CCTM-$V_bI_c$** inserted in a bilayer of DPhPC. The peptide chains are represented with transparent ribbons, lumenal residue side chains with sticks and water molecules and ions as spheres, the phosphorus of the lipid bilayer is represented with blue spheres.

**References**


1 Fong, J. H., Keating, A. E. & Singh, M. Predicting specificity in bZIP coiled-coil protein interactions. *Genome Biol.* **5**, (2004).

2 Thomson, A. R. *et al.* Computational design of water-soluble alpha-helical barrels. *Science* **346**, 485-488, (2014).

3 Šali, A. & Blundell, T. L. Comparative Protein Modelling by Satisfaction of Spatial Restraints. *J. Mol. Biol.* **234**, 779-815, (1993).

4 Emsley, P., Lohkamp, B., Scott, W. G. & Cowtan, K. Features and development of Coot. *Acta. Crystallogr. D* **66**, 486-501, (2010).

5 Thomas, F. *et al.* De Novo-Designed α-Helical Barrels as Receptors for Small Molecules. *ACS Synth. Biol.* **7**, 1808-1816, (2018).

6 Olsson, M. H. M., Søndergaard, C. R., Rostkowski, M. & Jensen, J. H. PROPKA3: Consistent Treatment of Internal and Surface Residues in Empirical pKa Predictions. *J. Chem. Theory Comput.* **7**, 525-537, (2011).

7 AMBER 2017 (University of California, San Francisco, 2017).

8 Maier, J. A. *et al.* ff14SB: Improving the Accuracy of Protein Side Chain and Backbone Parameters from ff99SB. *J. Chem. Theory Comput.* **11**, 3696-3713, (2015).

9 Salomon-Ferrer, R., Götz, A. W., Poole, D., Le Grand, S. & Walker, R. C. Routine Microsecond Molecular Dynamics Simulations with AMBER on GPUs. 2. Explicit Solvent Particle Mesh Ewald. *J. Chem. Theory Comput.* **9**, 3878-3888, (2013).

10 Roe, D. R. & Cheatham, T. E. PTRAJ and CPPTRAJ: Software for Processing and Analysis of Molecular Dynamics Trajectory Data. *J. Chem. Theory Comput.* **9**, 3084-3095, (2013).

11 Humphrey, W., Dalke, A. & Schulten, K. VMD: Visual molecular dynamics. *J. Mol. Graph.* **14**, 33-38, (1996).

12 Rao, S., Klesse, G., Stansfeld, P. J., Tucker, S. J. & Sansom, M. S. P. A BEST example of channel structure annotation by molecular simulation. *Channels* **11**, 347-353, (2017).

13 Jo, S., Kim, T. & Im, W. Automated Builder and Database of Protein/Membrane Complexes for Molecular Dynamics Simulations. *Plos One* **2**, (2007).

14 Huang, J. *et al.* CHARMM36m: an improved force field for folded and intrinsically disordered proteins. *Nat. Methods.* **14**, 71-73, (2017).

15 Lomize, M. A., Pogozheva, I. D., Joo, H., Mosberg, H. I. & Lomize, A. L. OPM database and PPM web server: resources for positioning of proteins in membranes. *Nucleic Acids Res.* **40**, D370-D376, (2012).

16 Wood, C. W. & Woolfson, D. N. CCBuilder 2.0: Powerful and accessible coiled-coil modeling. *Protein Sci.* **27**, 103-111, (2018).

17 Jurrus, E. *et al.* Improvements to the APBS biomolecular solvation software suite. *Protein Sci.* **27**, 112-128, (2018).

18 Callenberg, K. M. *et al.* APBSmem: A Graphical Interface for Electrostatic Calculations at the Membrane. *Plos One* **5**, (2010).

19 Kučerka, N., Nieh, M.-P. & Katsaras, J. Fluid phase lipid areas and bilayer thicknesses of commonly used phosphatidylcholines as a function of temperature. *Biochim. Biophys. Acta, Biomembranes* **1808**, 2761-2771, (2011).

20 Bellemare, F. & Fragata, M. Polarity Studies on the Head Group of Single-Layered Phosphatidylcholine-Alpha-Tocopherol Vesicles. *J. Colloid. Interf. Sci.* **77**, 243-252, (1980).
21 Kukic, P. *et al*. Protein Dielectric Constants Determined from NMR Chemical Shift Perturbations. *J. Am. Chem. Soc.* **135**, 16968-16976, (2013).
22 De Jesus, A. J. & Allen, T. W. The role of tryptophan side chains in membrane protein anchoring and hydrophobic mismatch. *Biochim. Biophys. Acta, Biomembranes* **1828**, 864-876, (2013).
23 Marcoline, F. V., Bethel, N., Guerriero, C. J., Brodsky, J. L. & Grabe, M. Membrane Protein Properties Revealed through Data-Rich Electrostatics Calculations. *Structure* **23**, 1526-1537, (2015).
24 Swanson, J. M. J., Wagoner, J. A., Baker, N. A. & McCammon, J. A. Optimizing the Poisson Dielectric Boundary with Explicit Solvent Forces and Energies: Lessons Learned with Atom-Centered Dielectric Functions. *J. Chem. Theory Comput.* **3**, 170-183, (2007).
25 Roux, B. Valence selectivity of the gramicidin channel: A molecular dynamics free energy perturbation study. *Biophys. J.* **71**, 3177-3185, (1996).
26 Hille, B. *Ion channels of excitable membranes*. 3rd edn, (Sinauer, 2001).
27 Woolley, G. A. *et al*. Intrinsic rectification of ion flux in alamethicin channels: studies with an alamethicin dimer. *Biophys. J.* **73**, 770-778, (1997).
28 Dieckmann, G. R. *et al*. Exploration of the Structural Features Defining the Conduction Properties of a Synthetic Ion Channel. *Biophys. J.* **76**, 618-630, (1999).
29 Smart, O. S., Neduvelil, J. G., Wang, X., Wallace, B. A. & Sansom, M. S. P. HOLE: A program for the analysis of the pore dimensions of ion channel structural models. *J. Mol. Graph.* **14**, 354-360, (1996).
30 Noskov, S. Y., Im, W. & Roux, B. Ion Permeation through the α-Hemolysin Channel: Theoretical Studies Based on Brownian Dynamics and Poisson-Nernst-Plank Electrodiffusion Theory. *Biophys. J.* **87**, 2299-2309, (2004).
31 Furini, S., Zerbetto, F. & Cavalcanti, S. Application of the Poisson-Nernst-Planck Theory with Space-Dependent Diffusion Coefficients to KcsA. *Biophys. J.* **91**, 3162-3169, (2006).
32 Liebschner, D. *et al*. Polder maps: improving OMIT maps by excluding bulk solvent. *Acta. Crystallogr. D* **73**, 148-157, (2017).
33 Hummer, G., Rasaiah, J. C. & Noworyta, J. P. Water conduction through the hydrophobic channel of a carbon nanotube. *Nature* **414**, 188-190, (2001).
34 Beckstein, O. & Sansom, M. S. P. Liquid-vapor oscillations of water in hydrophobic nanopores. *Proc. Natl. Acad. Sci. U.S.A* **100**, 7063-7068, (2003).
35 Aryal, P., Sansom, M. S. P. & Tucker, S. J. Hydrophobic Gating in Ion Channels. *J. Mol. Biol.* **427**, 121-130, (2015).
36 Walshaw, J. & Woolfson, D. N. SOCKET: A program for identifying and analysing coiled-coil motifs within protein structures. *J. Mol. Biol.* **307**, 1427-1450, (2001).